Monthly Notices of the ROYAL ASTRONOMICAL SOCIETY

MNRAS **507,** 4102–4119 (2021) https://doi.org/10.1093/mnras/stab2001
Advance Access publication 2021 July 15

High-resolution spectroscopic follow-up of the most metal-poor candidates from SkyMapper DR1.1

D. Yong [1,2]★ G. S. Da Costa [1,2] M. S. Bessell [1] A. Chiti,[3] A. Frebel,[3] X. Gao [4] K. Lind,[5] A. D. Mackey [1] A. F. Marino [6] S. J. Murphy [7] T. Nordlander [1,2] M. Asplund, A. R. Casey [2,8] C. Kobayashi,[2,9] J. E. Norris[1] and B. P. Schmidt[1]

[1]*Research School of Astronomy and Astrophysics, Australian National University, Canberra, ACT 0200, Australia*
[2]*ARC Centre of Excellence for Astrophysics in Three Dimensions (ASTRO-3D), Canberra 2611, Australia*
[3]*Department of Physics and Kavli Institute for Astrophysics and Space Research, Massachusetts Institute of Technology, Cambridge, MA 02139, USA*
[4]*Max-Planck-Institut für Astronomie (MPIA), Königstuhl 17, D-69117 Heidelberg, Germany*
[5]*Department of Astronomy, Stockholm University, AlbaNova University Center, 106 91 Stockholm, Sweden*
[6]*Istituto Nazionale di Astrofisica – Osservatorio Astronomico di Arcetri, Largo Enrico Fermi, 5, I-50125 Firenze, Italy*
[7]*School of Science, The University of New South Wales, Canberra, ACT 2600, Australia*
[8]*School of Physics & Astronomy, Monash University, Wellington Road, Victoria, Clayton 3800, Australia*
[9]*Centre for Astrophysics Research, Department of Physics, Astronomy and Mathematics, University of Hertfordshire, Hatfield AL10 9AB, UK*

Accepted 2021 July 12. Received 2021 July 11; in original form 2021 June 2

ABSTRACT

We present chemical abundances for 21 elements (from Li to Eu) in 150 metal-poor Galactic stars spanning $-4.1 <$ [Fe/H] < -2.1. The targets were selected from the SkyMapper survey and include 90 objects with [Fe/H] ≤ -3 of which some 15 have [Fe/H] ≤ -3.5. When combining the sample with our previous studies, we find that the metallicity distribution function has a power-law slope of $\Delta(\log N)/\Delta[\mathrm{Fe/H}] = 1.51 \pm 0.01$ dex per dex over the range $-4 \leq$ [Fe/H] ≤ -3. With only seven carbon-enhanced metal-poor stars in the sample, we again find that the selection of metal-poor stars based on SkyMapper filters is biased against highly carbon-rich stars for [Fe/H] > -3.5. Of the 20 objects for which we could measure nitrogen, 11 are nitrogen-enhanced metal-poor (NEMP) stars. Within our sample, the high NEMP fraction (55 per cent ± 21 per cent) is compatible with the upper range of predicted values (between 12 per cent and 35 per cent). The chemical abundance ratios [X/Fe] versus [Fe/H] exhibit similar trends to previous studies of metal-poor stars and Galactic chemical evolution models. We report the discovery of nine new r-I stars, four new r-II stars, one of which is the most metal-poor known, nine low-α stars with [α/Fe] ≤ 0.15 as well as one unusual star with [Zn/Fe] $= +1.4$ and [Sr/Fe] $= +1.2$ but with normal [Ba/Fe]. Finally, we combine our sample with literature data to provide the most extensive view of the early chemical enrichment of the Milky Way Galaxy.

Key words: stars: abundances – stars: Population II – Galaxy: abundances – early universe.

1 INTRODUCTION

The most metal-poor stars in the Galaxy provide a unique opportunity to understand the Milky Way's earliest stages of formation and evolution, and the origin of the chemical elements (Beers & Christlieb 2005; Frebel & Norris 2015). The basic assumptions are that the metallicity of a star serves as a proxy for its age (with iron as the canonical measure of metallicity) and that the atmospheres of low-mass stars retain the chemical composition of the interstellar medium at the time and place of their birth. In this context, chemical abundance studies of the most iron-poor stars probe the earliest chemical enrichment events and the properties of the previous generation(s) of stars.

The identification and analysis of the most iron-poor stars has been a major endeavour, since the discovery that some stars are metal deficient with respect to the sun (Chamberlain & Aller 1951; Baschek 1959; Wallerstein et al. 1963). Important advances have come from pushing to ever lower metallicity (e.g. Bessell & Norris 1984; Christlieb et al. 2002; Frebel et al. 2005; Caffau et al. 2011; Keller et al. 2014; Aguado et al. 2018; Starkenburg et al. 2018; Nordlander et al. 2019) in the pursuit of identifying a star whose chemical composition reflects the primordial big bang composition. Significant advances in our understanding of early chemical enrichment have come from studies which have sought to increase the numbers of known metal-poor stars and investigate their chemical abundance patterns (e.g. McWilliam et al. 1995; Ryan, Norris & Beers 1996; Johnson 2002; Cayrel et al. 2004; Venn et al. 2004, 2020; Aoki et al. 2006; Bonifacio et al. 2009, 2012; Yong et al. 2013a; Roederer et al. 2014; Hansen et al. 2015; Placco et al. 2015; Yoon et al. 2016; Aguado et al. 2019; Hansen et al. 2019; Caffau et al. 2020). In parallel, theoretical efforts to study the properties and nucleosynthetic yields of the first generations of stars have been crucial in our interpretation of chemical abundance ratios in metal-poor stars (e.g. Schneider et al. 2003; Karlsson 2006; Salvadori, Schneider & Ferrara 2007; Prantzos 2008; Kobayashi & Nakasato 2011; Nomoto, Kobayashi &

★ E-mail: david.yong@anu.edu.au

Tominaga 2013; Tominaga, Iwamoto & Nomoto 2014; Clarkson & Herwig 2020).

The current generation of surveys focusing on the discovery of metal-poor stars include Pristine (Starkenburg et al. 2017) and SkyMapper (Keller et al. 2007), both of which are deep photometric surveys employing narrow- to intermediate-band metallicity sensitive filters. As described in Da Costa et al. (2019), the 'commissioning-era' of the SkyMapper survey led to the discovery of the most iron-poor star known, SMSS J031300.36−670839.3 with [Fe/H] < -6.5 (3D, NLTE) (Keller et al. 2014; Bessell et al. 2015; Nordlander et al. 2017). Additional studies of metal-poor stars from the SkyMapper commissioning-era survey were reported by Jacobson et al. (2015), Howes et al. (2016), and Marino et al. (2019). From the SkyMapper 'main' survey, we have discovered SMSS J160540.18−144323.1 with the lowest detected iron measurement, [Fe/H] $= -6.2$ (1D, LTE) Nordlander et al. (2019). Collectively, the results from the SkyMapper survey have provided important new data for understanding the early evolution of our Galaxy (e.g. Chiti et al. 2021; Cordoni et al. 2021).

The aim of this paper is to present the high-resolution spectroscopic analysis for a sample of 150 stars selected from SkyMapper photometry that have been vetted using intermediate-resolution spectroscopy on the ANU 2.3m telescope (see Da Costa et al. 2019 for details). The paper is arranged as follows. In Section 2, we describe the sample selection, observations, and data reduction. In Section 3, we present the analysis. Section 4 includes our results and our conclusions are given in Section 5.

2 SAMPLE SELECTION, OBSERVATIONS, AND DATA REDUCTION

Targets were identified from the SkyMapper metallicity sensitive diagram, $m_i = (v - g)_0 - 1.5(g - i)_0$ versus $(g - i)_0$, then observed at intermediate resolution using the WiFeS (Dopita et al. 2010) integral field spectrograph at the ANU 2.3 m telescope. Further details on the photometric selection and WiFeS spectroscopy can be found in Da Costa et al. (2019). As described in Bessell (2007) and Norris et al. (2013a), a spectrophotometric flux fitting method was applied to the WiFeS spectra to obtain estimates of the effective temperature ($T_{\rm eff}$), surface gravity (log g) and metallicity ([Fe/H]).

The most promising candidates, i.e. the most metal poor based on the WiFeS spectra, were observed using the Magellan Inamori Kyocera Echelle (MIKE) spectrograph (Bernstein et al. 2003) at the Magellan Telescope in 2017 and 2018. Note that the WiFeS observations were continuously being obtained such that the best available targets for high-resolution observations were updated before each observing run. Depending on the observing conditions, spectra were obtained with either the 0.7 or 1.0 arcsec slits, resulting in spectral resolutions of $R = 35\,000$ in the blue and $R = 28\,000$ in the red, or $R = 28\,000$ in the blue and $R = 22\,000$ in the red, for the smaller and larger slit sizes, respectively. The CCD binning was set to 2×2. Exposure times were adjusted to achieve signal-to-noise ratios of around S/N = 50 per pixel near 4500Å. We examined the spectra at the telescope and in some instances we re-observed objects to increase the S/N. The average S/N is 54 per pixel near 4500Å and the minimum and maximum values are 19 and 138, respectively.

The spectra were reduced using the CarPy data reduction pipeline[1] described in Kelson (2003). Multiple exposures were combined and individual orders were merged and normalized to create a single continuous spectrum per star. For the continuum normalization, we applied two-dimensional modelling following the approach of Barklem et al. (2002) and Ramírez, Allende Prieto & Lambert (2008). That is, we fit high order polynomials to the fluxes in each order, as well as variations in the blaze perpendicular to the dispersion.

Note that two targets included in this study were not originally selected from the procedure described in Da Costa et al. (2019). SMSS J054913.80−453904.0 (= HE 0547−4539) is from Barklem et al. (2005) and SMSS J143511.34−420326.4 (= SMSS J1435−4203) is from Jacobson et al. (2015). Both objects were observed as bright back-up targets. At the time of the Magellan/MIKE observations, two of the candidates were not recognized as having published high-dispersion analyses: SMSS J030428.44−340604.8 (= HE 0302−3417A) and SMSS J232121.57−160505.4 (= HE 2318−1621) were studied by Hollek et al. (2011) and Placco et al. (2014a), respectively. We have retained them in our analysis and briefly discuss comparisons with published data at the end of Section 3. (We also observed SMSS J100231.91−461027.5 which is a likely post-AGB star.)

Three candidates were observed using the HIRES spectrograph (Vogt et al. 1994) at the Keck telescope on 02 Feb 2017. We used the red cross disperser and the C1 decker with a slit width of 0.86 arcsec that provides a spectral resolution of $R = 45\,000$. The CCD binning was 2×1 (spatial × spectral). The data were reduced using MAKEE[2] and the wavelength coverage was from 4060 to 8350Å. The S/N ratios per pixel near 4500Å ranged from 29 to 79.

The final set of 48 candidates were observed using the FEROS spectrograph (Kaufer et al. 1999) at the ESO 2.2m telescope in May 2018. The FEROS spectra were processed automatically using the ESO online real-time pipeline reduction. The spectral resolution was $R = 48\,000$, CCD binning was 1×1 and wavelength coverage was from 3600 to 9100Å. The S/N ranged from 5 to 79 per pixel near 4500Å with an average value of 17. As we shall discuss later, we present stellar parameters (including [Fe/H]) for all stars but for the nine objects with S/N < 10 we do not measure chemical abundance ratios ([X/Fe]). The programme stars and observing details are presented in Table 1.

3 ANALYSIS

The stellar parameters were derived using the same approach as described in Norris et al. (2013a) and Yong et al. (2013a) to ensure that the current study is on the same scale and that the two samples can be combined. Effective temperatures ($T_{\rm eff}$) were from the spectrophotometric fits to the WiFeS spectra but adjusted by +50K for the following reason. In Norris et al. (2013a), $T_{\rm eff}$ was the mean from the spectrophotometric flux fitting method, Balmer line profiles and an empirical relation between the H_δ index HP2 and $T_{\rm eff}$ from the infrared flux method (Casagrande et al. 2010), red giants from Cayrel et al. (2004) and from Norris et al. (2013a). In that study, the effective temperatures from the spectrophotometric flux fitting method were, on average, 50K cooler than the mean value. Therefore in the present work, we increase those values by 50K to be on the same scale.

As in Yong et al. (2013a), surface gravities (log g) were adopted from the Y^2 isochrones (Demarque et al. 2004) assuming an age of 13 Gyr and [α/Fe] $= +0.3$. For five objects, the spectrophotometric flux fitting indicated surface gravities that were inconsistent with being red giant branch stars. These five stars are horizontal branch

[1] https://code.obs.carnegiescience.edu/mike

[2] https://sites.astro.caltech.edu/~tb/makee/

Table 1. Programme stars and observing details.

ID SMSS	Telescope[a]	g (mag)	S/N[b]	JD	RV (km s^{-1})
J001604.23−024105.0	M	12.89	43	2458085.78715	49.3
J005420.96−844117.0	M	14.59	38	2458084.99471	182.8
J011126.27−495048.4	M	14.40	52	2458037.93753	255.0
J020050.19−465735.2	M	13.40	77	2458035.87291	−7.0
J024246.96−470353.6	M	14.90	42	2458086.04841	6.9
J030245.60−281454.0	M	14.19	52	2458187.75078	45.9
J030258.53−284326.9	M	14.29	54	2458188.76044	44.7
J030428.44−340604.8	M	11.13	138	2458084.73097	122.5
J030634.26−750133.3	M	14.12	88	2458035.74364	143.2
J030740.92−610018.8	M	14.80	54	2458035.54878	300.9

Notes. This table is published in its entirety in the electronic edition of the paper. A portion is shown here for guidance regarding its form and content.
[a]F = ESO 2.2m + FEROS; K = Keck + HIRES; M = Magellan + MIKE.
[b]Signal-to-noise ratio per pixel near 4500Å.

or asymptotic giant branch objects. For the remaining objects, the mean difference in surface gravity (high-resolution analysis − ANU 2.3 m) is +0.28 (σ = 0.37). We also checked our surface gravities by comparing against values obtained using *Gaia* EDR3 parallaxes (Gaia Collaboration et al. 2021), assuming a mass of 0.8 $M_{\odot}$. For objects with fractional errors in parallax <20 per cent, the difference in log g (this study − *Gaia*) is −0.19 (σ = 0.33). We regard the agreement as satisfactory given the 0.3 dex uncertainty in log g values from the spectrophotometric fits (Da Costa et al. 2019).

Model atmospheres were taken from the α-enhanced, [α/Fe] = +0.4, NEWODF grid of ATLAS9 models by Castelli & Kurucz (2003). These one-dimensional (1D), plane-parallel, local thermodynamic equilibrium (LTE) models were computed using a microturbulent velocity of 2 km s^{-1} and no convective overshooting. Using software described in Allende Prieto et al. (2004), we interpolated within the grid to produce models with the required $T_{\rm eff}$, log g and [M/H]. In Fig. 1 (left-hand panel), we present the location of the programme stars in the $T_{\rm eff}$ versus log g plane. For comparison, we also present the Norris et al. (2013a) sample in the right-hand panel. It is clear that the present sample consists entirely of evolved stars, i.e. objects on the red giant branch, horizontal branch, or asymptotic giant branch.

Equivalent widths were measured for a set of lines in all programme stars (see Table 2). The line list is identical to the one used in Norris et al. (2013a) and Yong et al. (2013a). Radial velocities (see Table 1) were measured by comparing the observed and predicted wavelengths of the lines for which equivalent widths were measured. The typical standard deviation was 0.5 km s^{-1}.

Using the LTE stellar line analysis programme MOOG (Sneden 1973; Sobeck et al. 2011), we computed abundances for Fe I and Fe II lines. The microturbulent velocity, ξ_t, was determined by forcing the abundances from Fe I lines to have no trend with the reduced equivalent width, log(W_{λ}/λ). The metallicity, [Fe/H], was inferred from Fe I lines. We recognize that Fe II lines are less affected by non-LTE effects (Asplund 2005; Bergemann et al. 2012; Lind, Bergemann & Asplund 2012; Amarsi et al. 2016). However, there are considerably fewer Fe II lines in the programme stars compared to the number of Fe I lines, and we were also interested in being consistent with the Yong et al. (2013a) study that adopted the same methodology.

We then compared the derived metallicity, [Fe/H], with the value assumed when generating the model atmosphere, [M/H]. If the difference exceeded 0.2 dex, we computed an updated model atmosphere with [M/H]$_{\rm new}$ = [Fe/H]$_{\rm star}$, and the surface gravity was re-computed (using isochrones as described above but with the updated metallicity). This process was repeated until the stellar parameters converged (usually within an iteration or two). During this process, we removed Fe I lines that differed from the median abundance by more than 0.5 dex or 3σ. Additionally, we were mindful that for the C-rich stars, some lines can be blended with CH so we repeated the entire analysis using a set of lines which we believe are free from CH blending (Norris et al. 2007, 2010). Those stars are identified in Table 3 as 'C-rich = 1'. Stellar parameters are presented in Table 3.

Recall that some nine stars have S/N < 10. While we present radial velocities and stellar parameters for those objects, we do not present chemical abundances. Additionally, there are nine objects that were observed with multiple telescopes. Seven of these stars were observed with FEROS and MIKE. We present their stellar parameters and radial velocities separately in Tables 1 and 3. For the chemical abundance ratios, however, we only provide measurements from the higher quality MIKE spectra. Two of these stars were observed with HIRES and MIKE. We provide stellar parameters and chemical abundances separately, and use the average values in the figures.

The spectra of a number of cooler stars, despite being 'C-normal', i.e. not enhanced in C ([C/Fe] < 0.7), nevertheless show numerous strong CH lines that could potentially blend and contaminate the atomic lines. To identify those stars, we utilized the spectrum synthesis of the CH G band near 4300Å as described later in this section. We identified a CH feature near 4323Å and selected a threshold depth of 0.75 relative to the continuum. For any star in which the best-fitting synthetic spectrum reached a depth greater than 0.75, we analysed that object using the CH clean line list. Those stars are flagged in Table 3 with '*G*-band strength = 1', and there are 21 such objects in the sample. The final stellar parameters are presented in Table 3 where for the stars that are C-rich or have strong *G*-band strengths, we adopted the results from the CH-clean line list.

In Fig. 2, we compare the metallicities from the spectrophotometric flux fitting method using the WiFeS spectra and from the analysis of the high dispersion spectra. The metallicities from the high dispersion spectra are, on average, 0.30 ± 0.03 (σ = 0.33) dex higher than the values from the WiFeS spectra. While this difference is slightly larger than the value reported in Da Costa et al. (2019) of 0.04 ± 0.07 (σ = 0.38) dex, we reiterate that the metallicities from the WiFeS spectra are quantized at the 0.25 dex level (in some cases multiple observations were averaged). While we increased $T_{\rm eff}$ by

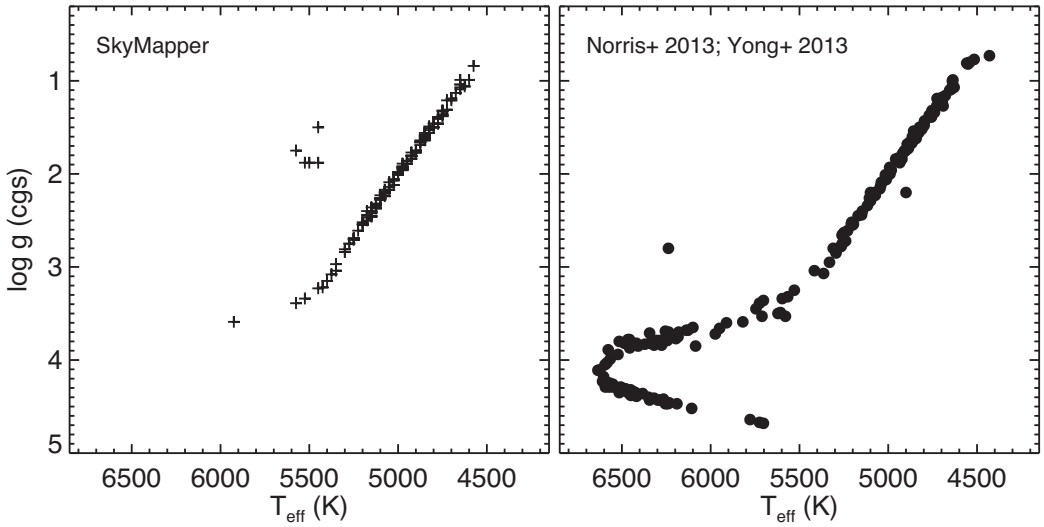

Figure 1. $T_{\rm eff}$ versus log g for the current SkyMapper sample (left) and for the Norris et al. (2013a) and Yong et al. (2013a) sample (right).

Table 2. Line list and equivalent width measurements.

Wavelength (Å)	Species	LEP (eV)	log *gf*	EW (mÅ)	EW (mÅ)
				0016–0241	0054–8441
5889.95	11.0	0.00	0.10	107.8	83.2
5895.92	11.0	0.00	−0.19	82.2	53.0
3829.36	12.0	2.71	−0.21	117.4	–
3832.30	12.0	2.71	0.15	152.2	–
3838.29	12.0	2.72	0.41	–	–
4571.10	12.0	0.00	−5.39	17.4	–
5172.68	12.0	2.71	−0.38	145.5	108.1
5183.60	12.0	2.72	−0.16	151.9	118.5
5528.41	12.0	4.34	−0.34	28.7	–
3944.01	13.0	0.00	−0.64	113.5	53.9

Note. This table is published in its entirety in the electronic edition of the paper. A portion is shown here for guidance regarding its form and content.

50K, the impact upon [Fe/H] is only +0.03 dex and cannot explain the +0.30 dex difference in metallicity.

Element abundances were determined from the measured equivalent widths using MOOG. Lines of Sc II, Mn I, Co I, and Ba II are affected by hyperfine splitting and we used data from Kurucz & Bell (1995) in our analysis. Ba II lines are also affected by isotopic splitting and we assumed the *r*-process isotopic composition and hyperfine splitting from McWilliam (1998). For Eu II lines, we also included isotopic and hyperfine splitting from Lawler et al. (2001).

For Li, C, and N, we measured abundances via spectrum synthesis of the 6707.8Å Li I line, the (0–0) and (1–1) bands of the $A-X$ electronic transitions of the CH molecule (4290–4330Å) and the NH molecule (3350–3370Å), respectively. We computed synthetic spectra using MOOG and adjusted the abundance until the observed and synthetic spectra were in agreement (see Figs 3 and 4). The broadening was determined using a Gaussian that represents the combined effects of the instrumental profile, atmospheric turbulence and stellar rotation. The typical uncertainties in the A(Li), [C/Fe] and [N/Fe] abundances are 0.2, 0.3, and 0.4 dex, respectively.

For a subset of objects we used spectrum synthesis to measure abundances for the following species: Zn I (4722.16, 4810.53Å), Y II (4398.01, 4883.68, 4900.12Å), Zr II (3998.96, 4149.20, 4156.27, 4208.98Å), and/or Eu II (4129.72, 4205.04Å). The typical uncertainties in the [X/Fe] ratios for Zn, Y, Zr, and Eu are 0.2, 0.2, 0.15, and 0.3 dex, respectively. We note that the numbers of stars in which we could measure Zn, Y, Zr, and Eu abundances were 35, 23, 27, and 26, respectively. Given that we were unable to measure these elements in the majority of stars, we defer the discussion of those abundances until Section 4.4.

As with the analysis of Fe lines, we were careful to avoid blending from CH lines for C-rich stars or those with strong *G*-band strengths. Therefore, we repeated the analysis of atomic lines using a line list that was unaffected by CH lines and the stellar parameters determined from a similarly CH-free line list. The abundance ratios are presented in Tables 4–8, and we adopted the solar abundances from Asplund et al. (2009).

The chemical abundances are affected by uncertainties in the model atmospheres and we estimated those values to be $T_{\rm eff} \pm 100$K, log $g \pm 0.3$ dex, $\xi_t \pm 0.3$ km s^{-1}, and [M/H] ± 0.3 dex. We repeated the analysis varying the stellar parameters, one at a time, assuming that the errors are symmetric for positive and negative values. We present those uncertainties in Table 9 in which the final column is the accumulated error in which the four values are added in quadrature. To obtain the total error presented in Table 7, we update the random error in that table (s.e.$_{\log\epsilon}$[3]) by max(s.e.$_{\log\epsilon}$,0.20/$\sqrt{(N_{\rm lines})}$, where the second term is what would be expected for a set of $N_{\rm lines}$ with a dispersion of 0.20 dex (a conservative estimate for the abundance dispersion based on Fe I lines). The total error is obtained by adding this updated random error in quadrature with the error from the stellar parameters presented in Table 9.

For Fe and Ti, abundances have been obtained for the neutral and ionized species. By comparing those abundance ratios, any discrepancy could be attributed to non-LTE effects and/or errors in the surface gravity. For metal-poor stars, the LTE abundances obtained from neutral species are expected to be underestimated due to overionization (Thévenin & Idiart 1999; Mashonkina et al. 2011; Bergemann et al. 2012; Lind et al. 2012). That is, we would expect that neglecting non-LTE corrections might lead to negative values of [Fe I/H] − [Fe II/H] and [Ti I/H] − [Ti II/H]. In Fig. 5, we present the differences between the abundances from Fe I and Fe II lines (upper left-hand panel) and from Ti I and Ti II lines (lower left-hand panel).

[3]Standard error of the mean.

Table 3. Model atmosphere parameters.

ID SMSS	Telescope	$T_{\rm eff}$ (K)	log g (cgs)	ξ_t (km s^{-1})	[M/H]$_{\rm model}$ (dex)	[Fe/H]$_{\rm derived}$ (dex)	C-rich[a]	CH[b]	Class
J001604.23−024105.0	M	5075	2.20	1.8	−3.1	−3.21	0	0	
J005420.96−844117.0	M	5275	2.75	1.3	−3.4	−3.51	0	0	
J011126.27−495048.4	M	5075	2.21	1.5	−3.0	−2.94	0	0	Fe-rich
J020050.19−465735.2	M	5050	2.09	1.8	−3.7	−3.66	0	0	
J024246.96−470353.6	M	4775	1.41	2.1	−3.0	−2.94	0	0	
J030245.60−281454.0	M	4775	1.39	2.1	−3.4	−3.50	0	0	
J030258.53−284326.9	M	5575	1.75	2.1	−2.7	−2.67	0	0	
J030428.44−340604.8	M	4750	1.32	2.2	−3.4	−3.26	0	0	NEMP
J030634.26−750133.3	M	5075	2.20	1.6	−3.2	−3.14	0	0	
J030740.92−610018.8	M	5025	2.06	1.9	−3.1	−3.09	0	0	
J030853.27−700140.1	M	4775	1.40	2.1	−3.2	−3.16	1	1	CEMP

Notes. This table is published in its entirety in the electronic edition of the paper. A portion is shown here for guidance regarding its form and content.
[a]0 = C-normal 1 = CEMP object adopting the Aoki et al. (2007) definition and 2 = C-rich when including the Placco et al. (2014b) corrections for the effect of evolutionary status on carbon abundances.
[b]0 = G-band maximum depth is ≥ 0.75 relative to the continuum and 1 = G-band maximum depth in the best-fitting synthesis near 4323Å is < 0.75 relative to the continuum.
[c]S/N < 10. We report $T_{\rm eff}$, log g, and [Fe/H], but no chemical abundance ratios.

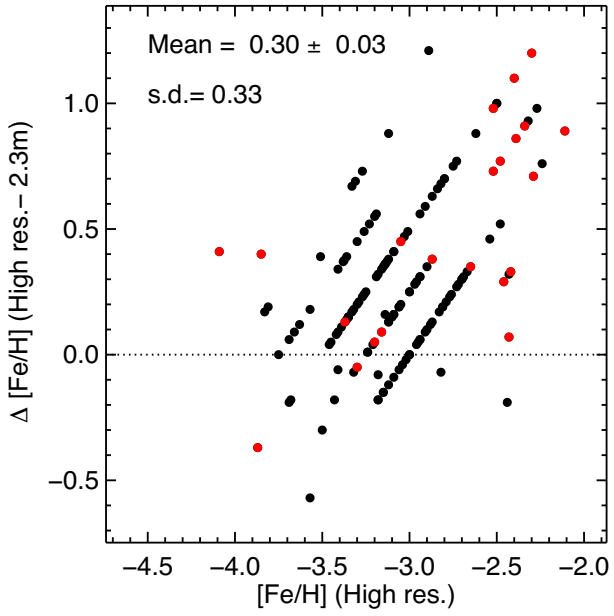

Figure 2. Comparison of the metallicities from the high-resolution spectra and the intermediate resolution ANU 2.3 m spectra. The red symbols are C-rich or those flagged with G-band strengths = 1. (Note that the 2.3 m metallicities are quantized at the 0.25 dex level, although in some cases multiple observations were averaged.)

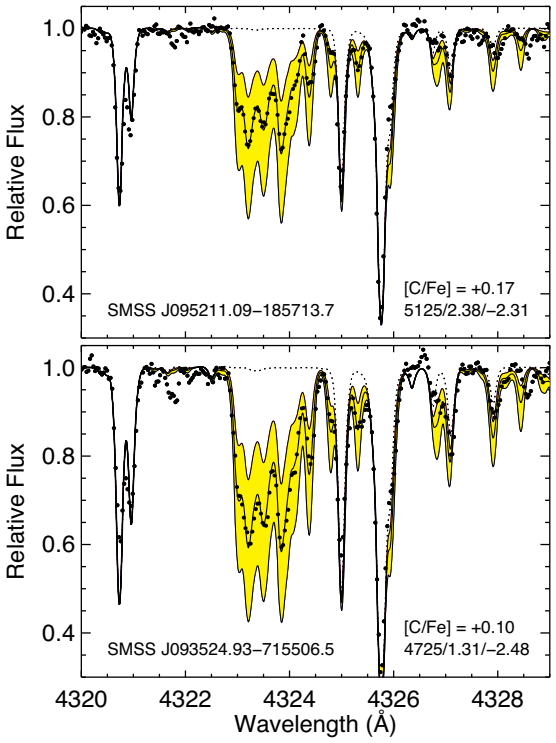

Figure 3. Comparison of observed (filled dots) and synthetic spectra in the region near 4325Å. Synthetic spectra with no C, [C/Fe] = −9, are shown as thin dotted lines. The best-fitting synthetic spectra are the thick black lines and the yellow shaded regions indicate ±0.3 dex from the best fit. The stellar parameters $T_{\rm eff}$/log g/[Fe/H] are shown.

We only consider stars with [Fe/H] ≤ −2.5 and that have two or more lines measured for a given species. For comparison, we show giants from the Norris et al. (2013a) and Yong et al. (2013a) sample in the right-hand panels. In all cases, the histograms are centred near zero. For Fe and Ti, while the abundances from neutral and ionized species are in good agreement, this does not imply that non-LTE effects can be neglected.

Four of the stars have been previously analysed. The objects are SMSS J054913.80−453904.0 (= HE 0547−4539) from Barklem et al. (2005), SMSS J143511.34−420326.4 (= SMSS J1435−4203) from Jacobson et al. (2015), SMSS J030428.44−340604.8 (= HE 03023−417A) from Hollek et al. (2011), and SMSS J232121.57−160505.4 (= HE 2318−1621) from Placco et al. (2014a).

Different approaches to determining $T_{\rm eff}$ and log g, as well as different line lists and log gf values result in systematic differences between the previous studies and this work. For example, for stars SMSS J054913.80–453904.0, SMSS J143511.34–420326.4, SMSS J030428.44–340604.8, and SMSS J232121.57–160505.4, we find

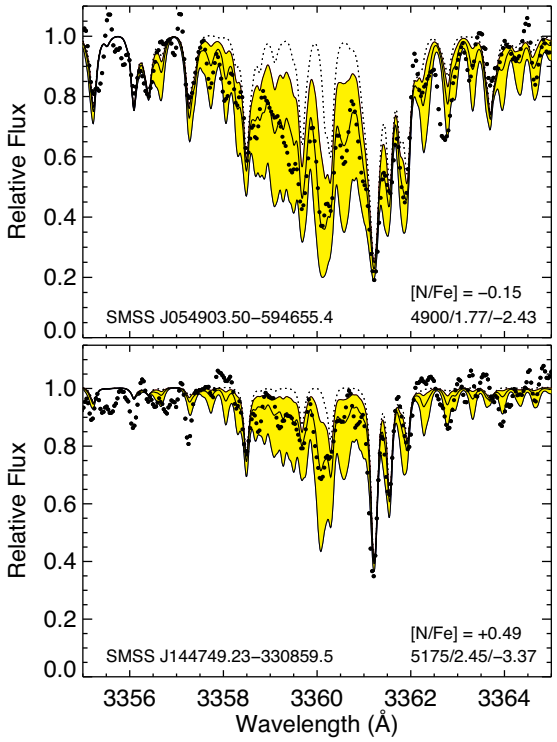

Figure 4. Same as Fig. 3 but for [N/Fe] in the region 3355–3365Å. The yellow shaded regions indicate ±0.5 dex from the best fit.

Table 4. Lithium abundances (note that this table excludes the majority of objects with no measurements).

ID	$A(Li)_{LTE}$	$A(Li)_{3D,\ NLTE}$[a]
SMSS J030634.26−750133.3	1.01	1.03
SMSS J034504.76−724732.2	1.51	1.56
SMSS J043800.94−831932.8	0.95	0.91
SMSS J044147.05−484842.9	1.12	1.14
SMSS J054903.50−594655.4	1.19	1.11
SMSS J062445.32−623003.7	1.28	1.28
SMSS J085210.25−761250.2	1.40	1.43
SMSS J103235.57−131520.2	1.05	1.07
SMSS J121709.12−272103.6	1.16	1.16
SMSS J125142.79−424304.4	1.13	1.15
SMSS J145536.24−340538.2	0.94	0.96
SMSS J154340.00−831819.5	1.12	1.06
SMSS J154634.19−081030.9	1.14	1.17
SMSS J163040.08−715639.1	1.21	1.27
SMSS J165512.00−725554.9	0.99	0.92
SMSS J172313.82−602320.6	1.00	0.98
SMSS J172604.29−590656.1	1.09	1.08
SMSS J212110.47−611758.9	0.99	1.01
SMSS J213402.81−622421.1	1.13	1.13
SMSS J214716.16−081546.9	0.95	0.97
SMSS J215842.28−202915.8	0.88	0.87

[a]3D NLTE corrections from Wang et al. (2021).

[Fe/H] = −3.15, −2.65, −3.26, and −3.03, while previous studies report [Fe/H] = −3.01, −3.15, −3.70, and −3.67, respectively.

We will not seek to understand the origin of any of these discrepancies in detail, merely noting that an advantage of our large and homogeneously analysed sample is that within it stars and their abundances can be readily compared with each other. However, we note that the average difference in [X/Fe] for these stars is generally small with the mean difference across 15 elements, in the sense (this work − literature) is −0.02 dex with a standard deviation of 0.32 dex.

Table 5. Carbon abundances and the corrections for evolutionary status from Placco et al. (2014b).

ID	A(C) (dex)	C_{corr} (dex)	$[C/Fe]_{corr}$ (dex)
SMSS J001604.23−024105.0	5.64	0.01	0.43
SMSS J005420.96−844117.0	<5.86	0.01	<0.95
SMSS J011126.27−495048.4	5.74	0.01	0.26
SMSS J020050.19−465735.2	5.33	0.01	0.57
SMSS J024246.96−470353.6	5.40	0.52	0.43
SMSS J030245.60−281454.0	<4.72	0.51	<0.30
SMSS J030258.53−284326.9	<6.41	0.20	<0.85
SMSS J030428.44−340604.8	5.12	0.57	0.52
SMSS J030634.26−750133.3	5.53	0.01	0.25
SMSS J030740.92−610018.8	5.82	0.02	0.50

Note. This table is published in its entirety in the electronic edition of the paper. A portion is shown here for guidance regarding its form and content.

Table 6. Nitrogen abundances (note that this table excludes the majority of objects with no measurements).

ID	A(N) (dex)	[N/Fe] (dex)	NEMP[a]
SMSS J030428.44−340604.8	5.35	0.78	1
SMSS J031703.94−374047.2	5.45	0.89	1
SMSS J052313.34−621822.5	5.85	0.78	1
SMSS J054650.97−471407.9	6.35	2.61	1
SMSS J054903.50−594655.4	5.25	−0.15	0
SMSS J054913.80−453904.0	4.95	0.27	0
SMSS J062445.32−623003.7	5.15	−0.25	0
SMSS J091043.10−144418.5	5.55	1.13	1
SMSS J095211.09−185713.7	4.95	−0.54	0
SMSS J095246.98−085554.0	5.05	0.09	0
SMSS J102410.14−082802.8	6.05	0.54	1
SMSS J103819.28−284817.9	5.25	1.11	1
SMSS J110901.23+075441.7	5.55	0.90	1
SMSS J121709.12−272103.6	4.95	−0.36	0
SMSS J144749.23−330859.5	4.95	0.49	0
SMSS J151044.04−395653.6	5.75	0.46	0
SMSS J181200.10−463148.8	5.55	1.02	1
SMSS J185358.63−555400.1	5.75	0.94	1
SMSS J190836.24−401623.5	6.15	1.65	1
SMSS J213402.81−622421.1	4.55	−0.16	0

[a]1 = NEMP object (Johnson et al. 2007) adopting the uncorrected C abundances.

4 RESULTS

4.1 MDF

The metallicity distribution function (MDF; usually based on Fe) is a crucial diagnostic tool for understanding low-mass star formation in the early universe. In Fig. 6, we plot the MDF for the current sample (left-hand panels) and the Norris et al. (2013a) and Yong et al. (2013a) sample (right-hand panels). In this figure, we also include SMSS J160540.18−144323.1 from Nordlander et al. (2019) with [Fe/H] = −6.2 that was discovered using SkyMapper DR 1.1 photometry. Unless explicitly mentioned otherwise, in the subsequent discussion we will not include this object. It is 2 dex more iron-poor than the next most iron-poor star in the sample, the observations and

Table 7. Chemical abundances (Na–Ba) for the programme stars.

ID	A(X)	$N_{\rm lines}$	s.e.$_{\log \epsilon X}$	[X/Fe]	Total error
Na I					
SMSS J001604.23−024105.0	3.04	2	0.08	0.00	0.11
SMSS J005420.96−844117.0	2.79	2	0.12	0.07	0.12
SMSS J011126.27−495048.4	3.10	2	0.14	−0.20	0.15
SMSS J020050.19−465735.2	–	–	–	–	–
SMSS J024246.96−470353.6	4.09	1	–	0.79	0.17
SMSS J030245.60−281454.0	3.40	2	0.07	0.66	0.14
SMSS J030258.53−284326.9	4.11	2	0.29	0.54	0.30
SMSS J030428.44−340604.8	2.81	2	0.07	−0.17	0.11
SMSS J030634.26−750133.3	2.91	2	0.06	−0.19	0.11
SMSS J030740.92−610018.8	3.04	2	0.13	−0.11	0.13

Note. This table is published in its entirety in the electronic edition of the paper. A portion is shown here for guidance regarding its form and content.

Table 8. Chemical abundances for Zn, Y, Zr, and Eu (note that this table excludes the majority of objects with no measurements).

ID	A(X)	$N_{\rm lines}$	s.e.$_{\log \epsilon X}$	[Eu/Fe]	Total error
Zn I					
SMSS J034749.80−751351.7	2.08	1	–	0.02	0.30
SMSS J043800.94−831932.8	1.94	1	–	0.38	0.30
SMSS J050247.62−642915.9	2.45	2	0.10	0.35	0.21
SMSS J052313.34−621822.5	2.19	1	–	0.39	0.30
SMSS J054903.50−594655.4	2.10	2	0.09	−0.03	0.21
SMSS J054913.80−453904.0	1.85	2	0.06	0.45	0.21
SMSS J062445.32−623003.7	2.04	1	–	−0.09	0.30
SMSS J072146.02−835759.7	2.44	2	0.04	−0.02	0.21
SMSS J084327.83−141513.3	2.68	2	0.03	1.41	0.21
SMSS J091117.11−264637.1	2.39	2	0.02	0.10	0.21

Note. This table is published in its entirety in the electronic edition of the paper. A portion is shown here for guidance regarding its form and content.

Table 9. Abundance errors from uncertainties in atmospheric parameters.

ID	Species	$\Delta T_{\rm eff}$ (+100 K)	$\Delta \log g$ (+0.3 dex)	$\Delta \xi_t$ (+0.3 km s^{-1})	Δ [M/H] (+0.3 dex)	Δ [X/Fe]
SMSS J001604.23−024105.0	Δ[Fe I/H]	0.06	−0.02	−0.09	0.01	0.11
SMSS J001604.23−024105.0	Δ[Fe II/H]	0.00	0.10	−0.02	0.00	0.10
SMSS J001604.23−024105.0	Δ[Fe/H]	0.06	−0.01	−0.09	0.01	0.10
SMSS J001604.23−024105.0	Δ[Na I/Fe]	−0.01	−0.02	−0.01	−0.01	0.02
SMSS J001604.23−024105.0	Δ[Mg I/Fe]	0.00	−0.05	−0.00	0.00	0.05
SMSS J001604.23−024105.0	Δ[A II/Fe]	−0.01	−0.02	−0.05	−0.01	0.06
SMSS J001604.23−024105.0	Δ[Si I/Fe]	0.01	−0.08	−0.04	0.00	0.09
SMSS J001604.23−024105.0	Δ[Ca I/Fe]	−0.02	0.00	0.05	0.00	0.05
SMSS J001604.23−024105.0	Δ[Sc II/Fe]	−0.03	0.10	−0.02	−0.01	0.11
SMSS J001604.23−024105.0	Δ[Ti I/Fe]	0.00	0.00	0.07	0.00	0.07
SMSS J001604.23−024105.0	Δ[Ti II/Fe]	−0.03	0.09	−0.01	−0.01	0.10
SMSS J001604.23−024105.0	Δ[Cr I/Fe]	0.00	0.00	0.03	−0.01	0.03
SMSS J001604.23−024105.0	Δ[Mn I/Fe]	0.01	−0.01	−0.02	−0.01	0.03
SMSS J001604.23−024105.0	Δ[Co I/Fe]	0.00	0.00	−0.00	−0.01	0.01
SMSS J001604.23−024105.0	Δ[Ni I/Fe]	0.01	0.00	−0.03	0.00	0.04
SMSS J001604.23−024105.0	Δ[Sr II/Fe]	−0.02	0.09	−0.10	0.00	0.14
SMSS J001604.23−024105.0	Δ[Ba II/Fe]	−0.02	0.11	0.07	0.00	0.13

Note. This table is published in its entirety in the electronic edition of the paper. A portion is shown here for guidance regarding its form and content.

analysis differ from the approach in this study, and only a handful of elements have abundance measurements. Nordlander et al. (2019) have already presented a comprehensive analysis and interpretation of this star. There are 91 stars with [Fe/H] ≤ -3.0 in the current sample of which 87 are newly reported objects; the other four known stars are SMSS J160540.18–144323.1 from Nordlander et al. (2019), SMSS J054913.80–453904.0 from Barklem et al. (2005), SMSS J030428.44–340604.8 from Hollek et al. (2011), and SMSS J232121.57–160505.4 from Placco et al. (2014a). For consistency, we have used our [Fe/H] determinations for the latter three stars:

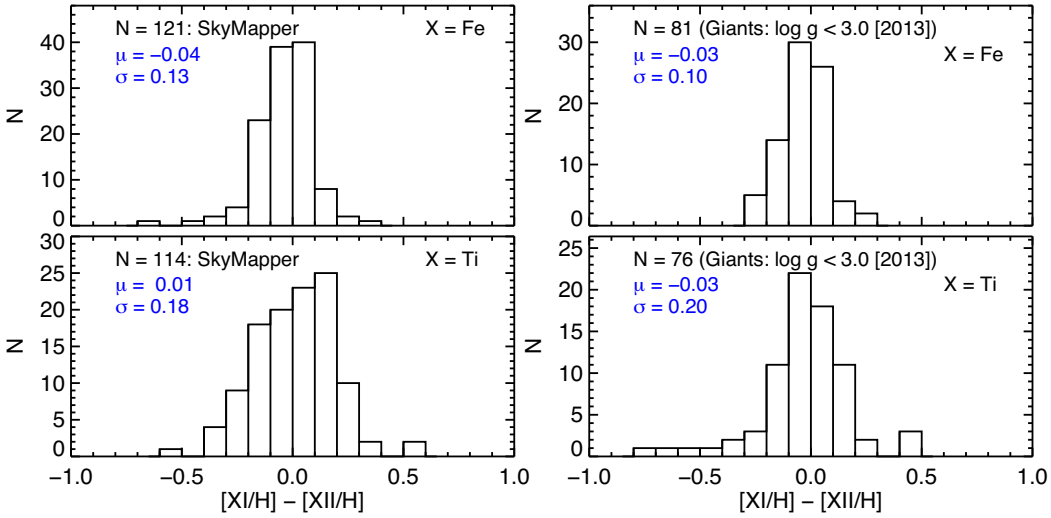

Figure 5. Histograms showing the abundance difference [Fe I/H] − [Fe II/H] (upper) and [Ti I/H] − [Ti II/H] (lower) for $N \geq 2$ lines and [Fe/H] ≤ -2.5. The current SkyMapper sample is shown in the left-hand panels and giants ($\log g < 3.0$) from the Norris et al. (2013a) and Yong et al. (2013a) sample in the right-hand panels. In each panel, we include the number of stars, mean (μ), and standard deviation (σ).

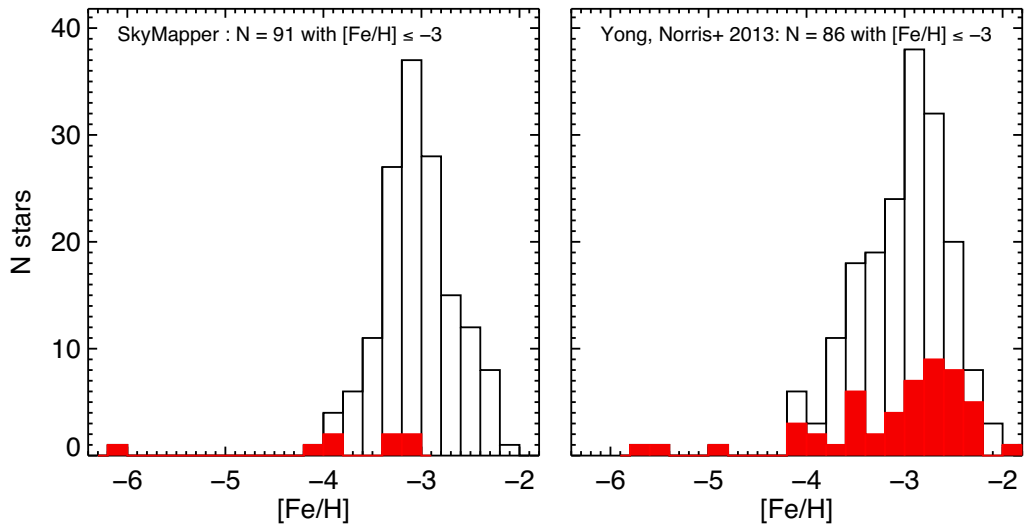

Figure 6. Metallicity distribution function for the current SkyMapper sample including SMSS J160540.18–144323.1 from Nordlander et al. (2019) (left) and for the Yong et al. (2013b) sample (right). The numbers of stars with [Fe/H] ≤ -3 are included in each panel and the red histogram indicates C-rich stars.

[Fe/H] = −3.15, −3.26, and −3.03, respectively. We emphasize that the two samples, this study and Norris et al. (2013a), are completely independent as the 2.3m follow-up observations of SkyMapper candidates has deliberately attempted to exclude previously known stars.

In order to combine the two samples, there are several considerations that need to be taken into account. For the Norris et al. (2013a) sample, the selection biases are described in Yong et al. (2013b; see their fig. 1). There were two main factors to consider. First, the Hamburg ESO Survey (HES) from which most targets were drawn is complete below [Fe/H] = −3.0 (Schörck et al. 2009; Li et al. 2010). Secondly, the ratio of HES candidates observed at high resolution relative to the total number of HES candidates as a function of metallicity needs to be included. That 'completeness function' was presented in Norris et al. (2013a).

For the current sample, candidates were first selected from the SkyMapper metallicity sensitive diagram, $m_i = (v - g)_0 - 1.5(g - i)_0$ versus $(g - i)_0$, as described in Da Costa et al. (2019). In principle, more metal-poor objects should have more negative values of m_i. However, Da Costa et al. (2019) showed that for objects with [Fe/H] ≤ -2.0, there was little correlation between the metallicity and the m_i value. That is, while the SkyMapper DR1.1 photometry is highly efficient at identifying stars with [Fe/H] < -2, it cannot readily discriminate between stars with [Fe/H] = −4 and [Fe/H] = −2 (the differences in the m_i values are smaller than the typical photometric errors). They also noted that large carbon enhancements can affect the m_i index making CEMP objects appear to be more metal rich. Below [Fe/H] = −4, Da Costa et al. (2019) suggest that C-rich stars do not fall outside of the photometric selection window. At [Fe/H] = −3.0, they suggest that is likely that some strongly C enhanced

objects will fall out of the selection box, although it is a 'complex function of effective temperature, [Fe/H] and [C/Fe], as well as of [N/Fe] and [O/Fe]' (Da Costa et al. 2019). Above about [Fe/H] = −3.5, the bias against C enhanced stars is clearly visible in Fig. 7, where there is a lack of C-rich stars in the current sample (left-hand panel) when compared to the previous sample (right-hand panel).

In the absence of further information (i.e. the SkyMapper selection bias, the [C/Fe] distribution as a function of $T_{\rm eff}$, log g and [Fe/H], and photometric uncertainties), we will cautiously proceed by producing a generalized histogram for the current sample and another for the 'completeness function' corrected sample from Norris et al. (2013a). That is, each data point is replaced by a unit Gaussian of width 0.15 dex. The Gaussians are summed to produce a realistically smoothed histogram. We normalize both histograms by the numbers of stars in each sample then combine the two distributions. The MDF for the combined sample (including SMSS J160540.18−144323.1 from Nordlander et al. 2019) is presented in Fig. 7 with linear (left) and logarithmic (right) scales.

For stars in the range $-4 \leq$ [Fe/H] ≤ -3, we fit the data using a linear function (right-hand panel) and find a power-law slope of Δ(log N)/Δ[Fe/H] = 1.51 ± 0.01 dex per dex. This slope is in excellent agreement with the value of 1.5[4] ± 0.1 in Da Costa et al. (2019), but considerably steeper than the canonical 1.0 from the Hartwick (1976) simple model. While we have yet to properly account for the impact of C-rich objects in the SkyMapper selection, our results reinforce how difficult it is to find stars more metal-poor than [Fe/H] = −3.0.

In creating this MDF from the combined sample, there are 177 stars (including SMSS J160540.18−144323.1) with [Fe/H] ≤ -3.0. We can compare the fractional uncertainty in the MDF from the Norris et al. (2013a) sample with the combined sample. That fractional uncertainty was obtained using the same approach described in Yong et al. (2013b). That is, using Monte Carlo simulations we replaced each data point with a random number drawn from a normal distribution of width 0.15 dex centred at the [Fe/H] of each star. We repeated this process for the entire sample and created a new generalized histogram. For 10 000 new random samples, we produced a generalized histogram for each random sample. Thus, at a given [Fe/H], we have a distribution of 10 000 values (one for each MDF), and we measured the FWHM of that distribution. That FWHM was taken as our estimate of the uncertainty in the MDF. For all values between $-4 \leq$ [Fe/H] ≤ -3, the fractional uncertainty in the MDF has improved with respect to the analysis in Yong et al. (2013b). At [Fe/H] = −4.0, the fractional uncertainty decreased by about 10 per cent. The greatest improvement was a ∼70 per cent decrease in the fractional uncertainty near [Fe/H] = −3.3.

In Fig. 7, the formal uncertainty on the slope is only 0.01. In the Monte Carlo approach described above, we fit each new MDF between $-4 \leq$ [Fe/H] ≤ -3 and find an average power-law slope of Δ(log N)/Δ[Fe/H] = 1.45 dex per dex with a standard deviation of 0.07 dex. We regard 0.07 dex as a more realistic estimate of the uncertainty in the MDF slope.

If we generate an MDF using the same approach described above but excluding the C-rich stars, the slope between $-4 <$ [Fe/H] < -3 is 1.74 ± 0.02. There are no C-normal stars substantially below [Fe/H] = −4, although we do not include the Caffau et al. (2011) star (which is a dwarf and the SkyMapper DR 1.1 sample is dominated by giants). In Fig. 6, C-rich stars are indicated by the red histogram and the MDF for those objects is considerably flatter than for the full sample.

[4]The slope was determined from stars in the range $-4.0 \leq$ [Fe/H] ≤ -2.75.

Youakim et al. (2020) presented the MDF of the Pristine survey based on a photometric sample of 80 000 main-sequence turn-off stars representative of the inner halo of the Galaxy (we overplot their data, corrected with their Gaussian mixture model and colour cuts and normalized at [Fe/H] = −3.05, in Fig. 7). Overall, they note that the MDF is not well represented by a single power law but in the metallicity range $-3.4 <$ [Fe/H] < -2.5, they find a slope of Δ(log N)/Δ[Fe/H] = +1.0 ± 0.1. While we would like to also examine our MDF over the same metallicity interval as Youakim et al. (2020), our sample is incomplete above [Fe/H] $\simeq -2.6$. That is, when generating an MDF using our combined sample, there is an artificial turnover near [Fe/H] $\simeq -2.6$. Therefore, we consider a slightly different metallicity range $-3.4 <$ [Fe/H] < -2.7, in which we find that our MDF has a slope of +1.07 ± 0.04 which is in excellent agreement with the Youakim et al. (2020) value.

Similarly, based on a large sample of candidate metal-poor giants selected from SkyMapper DR2 photometry (Onken et al. 2019), Chiti et al. (2021) find that the MDF in the metallicity range $-3.0 \leq$ [Fe/H] ≤ -2.3 is well-fit by a power law with a slope of Δ(log N)/Δ[Fe/H] = +1.53 ± 0.10.

In the metallicity range $-4.0 <$ [Fe/H] < -3.4, we find the MDF has a slope of 1.59 ± 0.02. Excluding C-rich stars, the slope increases to 2.11 ± 0.05. Again this is not dissimilar to the results of Youakim et al. (2020) who find a slope of +2.0 ± 0.2 for stars in their sample with [Fe/H] < -3.5 dex. Both studies (i.e. Youakim et al. and this work) agree on a significant change of slope somewhere around [Fe/H] = −3.5 to −4.

4.2 Li, C, and N

Lithium abundances, A(Li), were measured in 21 stars and are presented in Table 4. We include LTE and NLTE abundances where that latter makes use of corrections from Wang et al. (2021). None of the programme stars are enhanced in lithium.

Carbon abundance ratios are presented in Table 5 in which we list the evolutionary corrections from Placco et al. (2014b). We note in particular, that in order to enable a comparison with our previous work, we will utilize the uncorrected carbon abundances unless explicitly stated otherwise. In Fig. 8, we plot [C/Fe] versus [Fe/H] for the current sample (left) and the Norris et al. (2013a) and Yong et al. (2013a) sample (right). For the C-normal populations, the two samples exhibit similar behaviour. For the C-rich population, however, it is clear that the current sample lacks CEMP stars (only seven[5] are present plus a further 13 when taking into account evolutionary corrections[6]) as well as exhibiting a lack of stars with [C/Fe] substantially above +1.5. In contrast, in the right-hand panels of Fig. 8 there are some 31 CEMP stars with [C/Fe] $\geq +0.7$. The lack of very C enhanced stars among samples selected from SkyMapper photometry is particularly noticeable above [Fe/H] = −3.5 and this feature has been reported by Howes et al. (2015), Jacobson et al. (2015), and Marino et al. (2019). Possible reasons were touched on above and explored in more detail in Da Costa et al. (2019).

We now seek to compare the predicted and observed numbers of CEMP objects. Assuming uncorrected carbon abundances and the CEMP threshold of [C/Fe] $\geq +0.7$, Placco et al. (2014b) report

[5]The seven CEMP stars include six CEMP-no objects. The remaining object, SMSS J030853.27–700140.1, has [Ba/Fe] = +0.09 which does not allow it to be placed into any of the established sub-classes: CEMP-r, CEMP-s, CEMP-r/s, and CEMP-no.

[6]Those stars are identified in Table 3 as 'C-rich = 2'.

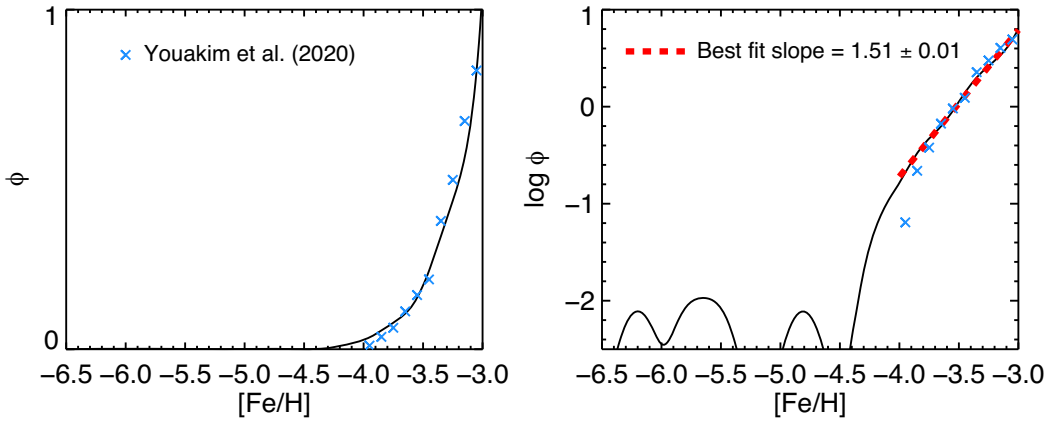

Figure 7. The metallicity distribution function in generalized histogram form (black lines) using linear (left) and logarithmic (right) scales for the combined sample (this study including SMSS J160540.18–144323.1 from Nordlander et al. (2019) plus Norris et al. 2013a). In the right-hand panel, we fit the slope between $-4 \leq$ [Fe/H] ≤ -3. In both panels, we overplot data from Youakim et al. (2020) (corrected with their Gaussian mixture model and colour cuts and normalized at [Fe/H] $= -3.05$) as blue crosses.

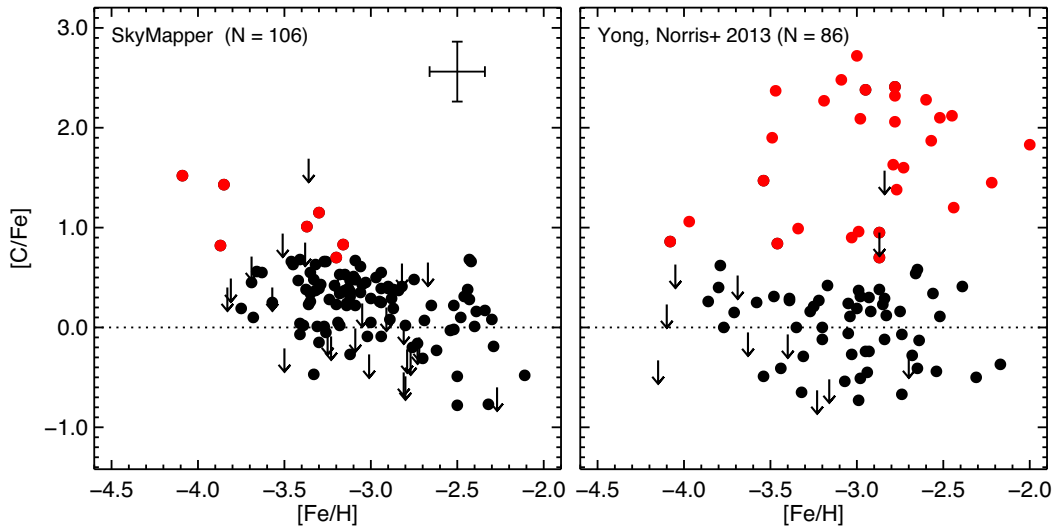

Figure 8. [C/Fe] versus [Fe/H] for the current SkyMapper sample (left) and giants ($\log g \leq 3.0$) from the Yong et al. (2013b) sample (right). The red symbols are C-rich objects and a representative error bar is included in the top right corner (left-hand panel). (All C abundances are 'observed', i.e. without correction for evolutionary status.)

cumulative CEMP frequencies for [Fe/H] ≤ -3.0, -3.5, and -4.0 of 32 per cent, 51 per cent, and 81 per cent, respectively. For our sample (including SMSS J160540.18−144323.1), the numbers of stars in those three metallicity regimes are 76, 16, and 2. Therefore, we would expect 24.3, 8.2, and 1.6 CEMP objects in the metallicity ranges [Fe/H] ≤ -3.0, -3.5, and -4.0, respectively. The numbers of CEMP stars in those metallicity ranges are 8, 4, and 2. Assuming Poisson statistics, for [Fe/H] ≤ -3.0 the lack of CEMP stars compared to the predicted number is significant at the 2.9σ level. For [Fe/H] ≤ -3.5, the difference between the predicted and observed numbers of CEMP stars represents only a 1.2σ result. Below [Fe/H] $= -4.0$, the statistics are small but the predicted and observed number of CEMP stars is in agreement.

When adopting the corrected carbon abundances and corresponding predictions from Placco et al. (2014b), the differences between the predicted and observed numbers of CEMP stars for [Fe/H] ≤ -3.0 and -3.5 are significant at the 2.1σ and 0.6σ levels, respectively (including SMSS J160540.18−144323.1). Therefore, any missing CEMP stars in our sample lie pre-dominantly in the range [Fe/H] > -3.5, which supports the discussion presented in Da Costa et al. (2019). We also note that Caffau et al. (2020) reported a smaller fraction of CEMP stars in their sample with [Fe/H] ≤ -2.5 (5 per cent; 3 out of 55) when compared to the Placco et al. (2014b) prediction of 19 per cent in that metallicity range.

Nitrogen abundances were measured in some 20 objects in the current sample with metallicities in the range $-4.1 \leq$ [Fe/H] ≤ -2.3. The [N/Fe] ratios range from -0.5 to $+2.6$. Among the sample, we identify 11 objects which are nitrogen-enhanced metal-poor (NEMP) stars as defined by Johnson et al. (2007) to have [N/Fe] $> +0.5$ and [C/N] < -0.5. One of these objects, SMSS J030428.44–340604.8, was studied by Hollek et al. 2011 but they did not report a N abundance. Among these 11 NEMP stars, two are enriched in Eu (r-I) and one is a CEMP-no object (SMSS J054650.97−471407.9 with [Fe/H] $= -4.09$). The metallicity distribution of the 11 NEMP stars (median [Fe/H] $= -3.27$) does not appear to be in any way different from the overall metallicity distribution of the sample.

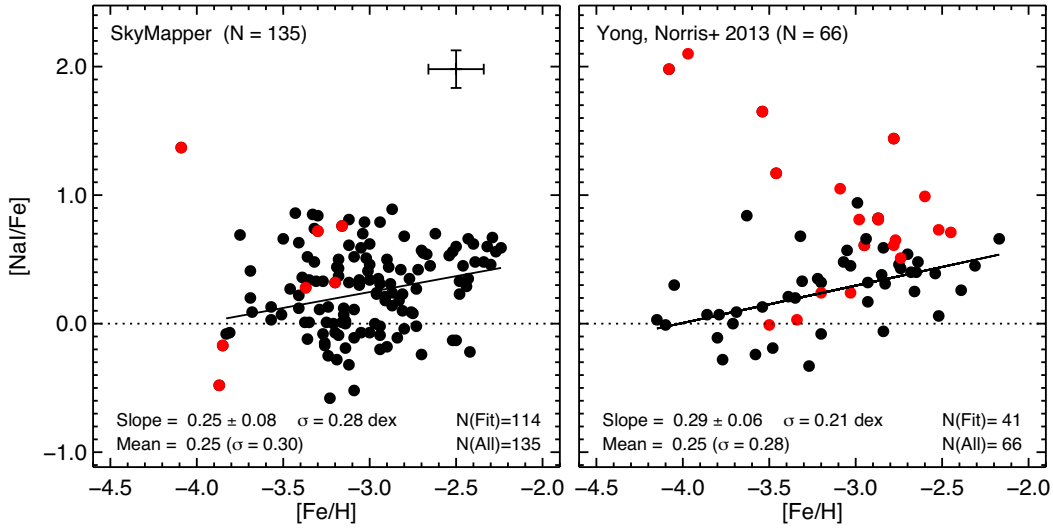

Figure 9. Same as Fig. 8 but for Na. The linear fit to the data excluding C-rich stars and 2σ outliers is included in each panel along with the slope, uncertainty, dispersion about the linear fit, mean, and standard deviation.

Internal mixing could decrease C and increase N (Spite et al. 2005; Placco et al. 2014b), which would reduce the NEMP fraction in our sample. If the corrected [C/N] ratio becomes ∼0, then these stars could be explained by the same scenario for CEMP-no stars, i.e. faint supernovae; the C/N ratios decrease with stellar rotation or any hydrogen mixing during stellar evolution of the progenitor massive stars (e.g. Nomoto et al. 2013). However, it is likely that our NEMP fraction remains high; for example, the evolutionary corrections to the observed C abundance for the NEMP stars SMSS J054650.97–471407.9 and SMSS J102410–082802.8 are negligible (see Table 5) so that the NEMP status of these stars remains unaffected by evolutionary corrections.

The NEMP population are believed to have formed via a similar process to the CEMP-*s* stars, namely accretion from an asymptotic giant branch (AGB) companion. The difference, however, is that sufficiently massive AGB companions synthesize more nitrogen than carbon, although it remains unclear, due to limitations in the modelling (e.g. see review by Karakas & Lattanzio 2014), whether extremely metal-poor massive AGB stars will also produce significant amounts of *s*-process material. We note, however, that none of our NEMP candidates show any evidence for potential *s*-process element enhancements. Specifically, the [Sr/Fe] and [Ba/Fe] abundance ratios for the NEMP stars are not distinguished from those for the bulk of the sample.

Based on modelling the mass distribution in AGB-star binaries, Johnson et al. (2007) predicted between 12 per cent and 35 per cent of their sample to be NEMP (i.e. between two and seven stars in their sample of 21 objects), but instead found zero. Subsequent studies have confirmed that NEMP stars are rare, e.g. Simpson & Martell (2019) reported only 80 such objects among the many thousands of metal-poor stars in the SAGA database (Suda et al. 2008). We are therefore somewhat surprised to find 11 NEMP stars among our sample; with only 20 objects with nitrogen measurements, the NEMP fraction is 55 per cent ± 21 per cent. It is unclear why we have been so successful in finding these rare stars. Given the low S/N near the NH lines at 3360Å, we were unable to measure N for the majority of our sample. Therefore, the 11 NEMP stars is a lower limit. Johnson et al. (2007) predict NEMP fractions between 12 per cent and 35 per cent, and our value is consistent with the upper range of the predictions.

4.3 Na to Ba

For the elements from Na to Ba, we plot the abundance distributions for three representative elements Na (odd-*Z* element), Ca (α element), and Ba (neutron-capture element) in Figs 9, 10, and 11. In each panel, we include the linear fit to the data excluding C-rich objects and 3σ outliers. The slope and uncertainty of the linear fit, the dispersion about the fit, the mean and standard deviation are included in each figure. In the right-hand panels of those figures, we also include the giant stars from the Norris et al. (2013a) and Yong et al. (2013a) sample. For all elements, the current sample exhibits very similar behaviour to the Norris et al. (2013a) sample.

In Fig. 12, we combine the current sample with Norris et al. (2013a), Jacobson et al. (2015), and Marino et al. (2019), where we plot stars with [Fe/H] ≤ -1.5 and $\log g < 3$. We again represent the data using generalized histograms of width 0.15 dex for [Fe/H] and 0.30 dex for [X/Fe]. The total sample includes 479 stars of which 220 lie below [Fe/H] $= -3$, 128 have [Fe/H] ≤ -3.25, 56 have [Fe/H] ≤ -3.5, 29 have [Fe/H] ≤ -3.75, and 10 have [Fe/H] ≤ -4.0, although not every element is measured in every star. While there are selection biases associated with each of the individual samples, we believe that this figure provides the most extensive view to date of the early chemical enrichment of the Milky Way Galaxy. The filled circles plotted at [Fe/H] $= -4$, -3.5, -3.0, -2.5, and -2.0 in each of the panels of Fig. 12 represent the average [X/Fe] ratios in the ranges, [Fe/H] ≤ -3.75, $-3.75 <$ [Fe/H] ≤ -3.25, $-3.25 <$ [Fe/H] ≤ -2.75, $-2.75 <$ [Fe/H] ≤ -2.25, and [Fe/H] > -2.25, respectively. We present those values as columns A, B, C, D, and E in Table 10.

It is clear from that figure that elements such as Ca, Ti, Cr, and Ni have significantly smaller dispersion when compared to C, N, Na, Sr, and Ba. For the former elements, the standard deviation for [X/Fe] in Fig. 12 is 0.16–0.18 dex. For the latter elements, the standard deviation is >0.35 dex. In particular, for the neutron-capture elements Sr and Ba, the ∼3 dex range in [X/Fe] at low metallicities is well known (e.g. McWilliam 1998, Roederer 2013). We note that the average uncertainties range from 0.05 dex (Cr and Ni) to 0.15 dex (Sr); that is, the observed standard deviation exceeds the average measurement uncertainty. The standard deviations for the

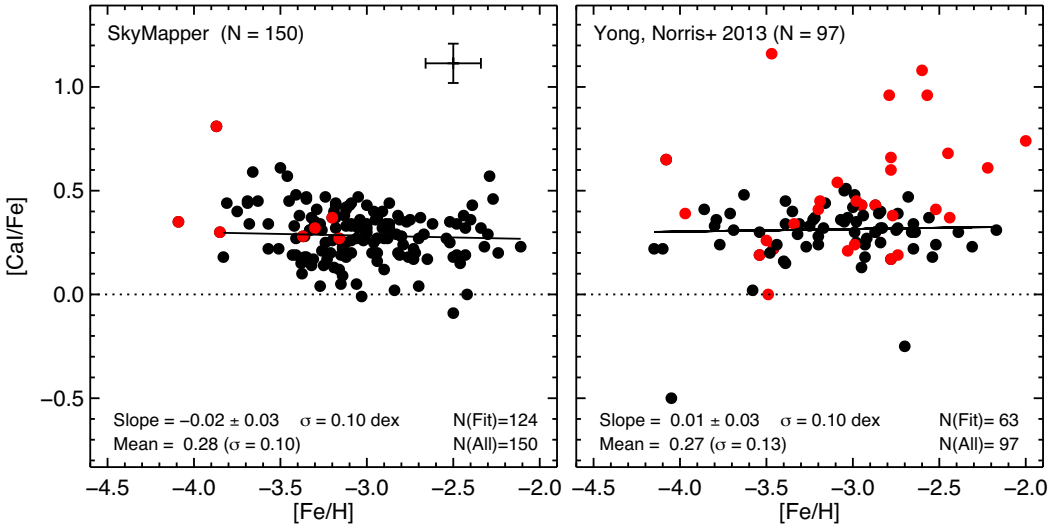

Figure 10. Same as Fig. 9 but for Ca.

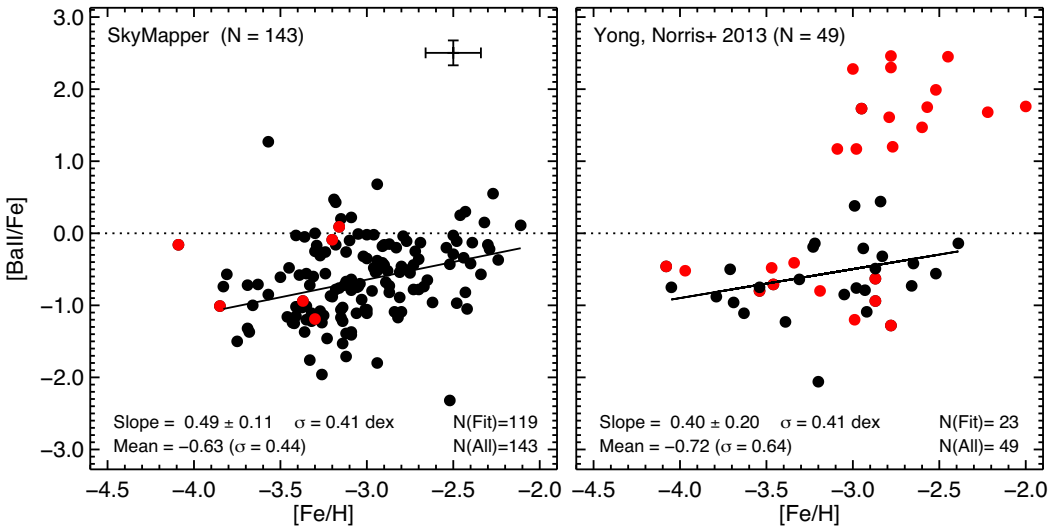

Figure 11. Same as Fig. 9 but for Ba.

other elements depicted lie between those for Ca, Ti, Cr, and Ni and those for C, N, Sr, and Ba, with typical values of 0.28 dex.

We note that while the trends in Fig. 12 are similar to those presented in other studies, Cayrel et al. (2004) and Reggiani et al. (2017) have achieved higher abundance precision and smaller dispersion when using higher quality spectra.

In Fig. 12, we also include predictions from a Galactic chemical evolution model by Kobayashi et al. (2020) (updated to include stellar rotation, Kobayashi et al. in preparation) as the dashed blue lines (these represent the average values in their solar neighbourhood model). In general, there is reasonable agreement between the observational data (1D LTE analysis) and the theoretical predictions. Notable exceptions include N, Sc, and Ti that are known to exhibit differences between theory and observations. The detailed discussion of the differences between the observations and the model can be found in Kobayashi et al. (2020), but briefly: the differences for Na, Al, Cr, and Co are potentially due to NLTE effects. Those for N and Ba can be solved with the inclusion of stellar rotation (e.g. Kobayashi, Karakas & Umeda 2011; Kobayashi et al. in preparation). Those for Sc and Ti might be solved with multidimensional effects, although there are no successful explosion models that can be used in galactic chemical evolution models.

4.4 Zn, Y, Zr, and Eu

We now consider Zn, Y, Zr, and Eu. In the previous subsections, we excluded these elements since we were unable to measure abundances in the majority of stars. (As noted earlier, Zn, Y, Zr and Eu abundances were only measured in 35, 23, 27, and 26 stars, respectively.)

In Fig. 13, there is a clear increase in [Zn/Fe] with decreasing [Fe/H]. That trend, however, is a direct consequence of the detection threshold for Zn. Following Roederer (2013), we computed approximate abundance thresholds corresponding to the detection of the 4810Å Zn I line for a representative giant star with $T_{\rm eff} = 4500$ K and $\log g = 1.5$ for metallicities ranging from [Fe/H] $= -5.0$ to -2.0 (in steps of 0.5 dex). The red dashed line in the left panel of Fig. 13 corresponds to a line strength of 10 mÅ. For example, at [Fe/H] $= -3.5$

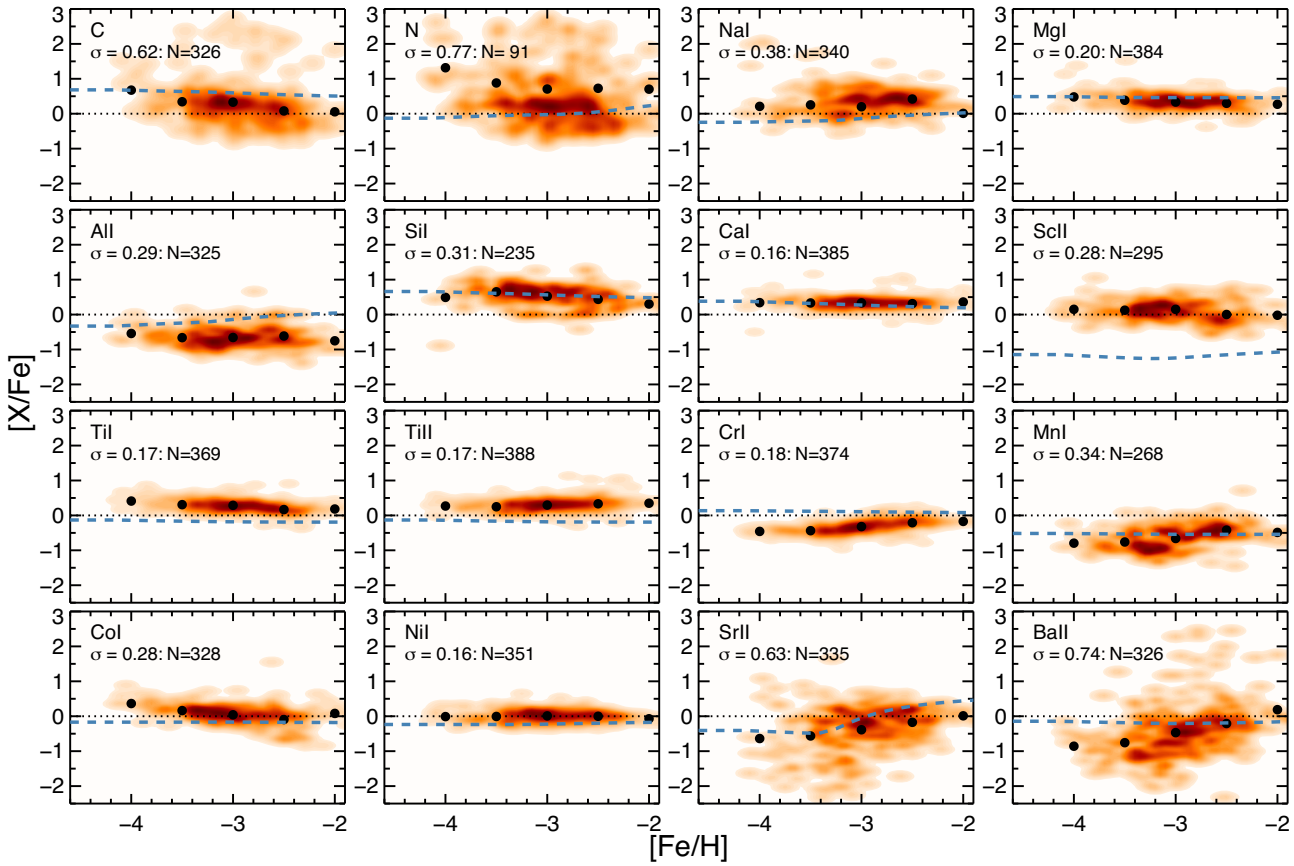

Figure 12. [X/Fe] versus [Fe/H] for the elements from C to Ba for the current SkyMapper sample, Norris et al. (2013a), Jacobson et al. (2015), and Marino et al. (2019). (Only stars with [Fe/H] ≤ -1.5 and $\log g < 3$ are included.) We represent the data using generalized histograms of width 0.15 dex for [Fe/H] and 0.30 dex for [X/Fe]. Average values are overplotted as filled circles and the dashed blue lines are predictions from a Galactic chemical evolution model by Kobayashi, Karakas & Lugaro (2020) updated to include stellar rotation (Kobayashi et al. in preparation).

Table 10. Mean [X/Fe] values in various metallicity ranges for the combined sample shown in Fig. 12. (A: [Fe/H] ≤ -3.75. B: $-3.75 <$ [Fe/H] ≤ -3.25. C: $-3.25 <$ [Fe/H] ≤ -2.75. D: $-2.75 <$ [Fe/H] ≤ -2.25. E: [Fe/H] > -2.25.)

Element	Mean [X/Fe]				
	A	B	C	D	E
C	0.68	0.34	0.33	0.08	0.05
N	1.32	0.88	0.71	0.73	0.70
Na I	0.21	0.25	0.20	0.42	0.01
Mg I	0.48	0.39	0.33	0.30	0.27
Al I	−0.54	−0.66	−0.66	−0.61	−0.75
Si I	0.49	0.65	0.53	0.44	0.30
Ca I	0.34	0.33	0.33	0.31	0.36
Sc II	0.15	0.12	0.15	0.00	−0.02
Ti I	0.41	0.31	0.29	0.17	0.18
Ti II	0.27	0.25	0.29	0.33	0.35
Cr I	−0.46	−0.44	−0.32	−0.21	−0.17
Mn I	−0.79	−0.76	−0.66	−0.42	−0.49
Co I	0.36	0.16	0.04	−0.10	0.08
Ni I	−0.01	−0.01	0.01	−0.00	−0.07
Sr II	−0.64	−0.56	−0.39	−0.17	0.01
Ba II	−0.86	−0.76	−0.47	−0.21	0.19

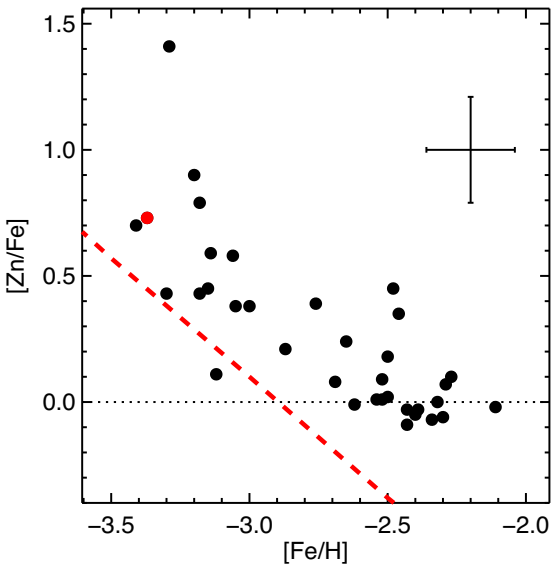

Figure 13. [Zn/Fe] versus [Fe/H]. The red symbol is a C-rich star. The red dashed line indicates the approximate detection threshold for the 4810Å Zn I line.

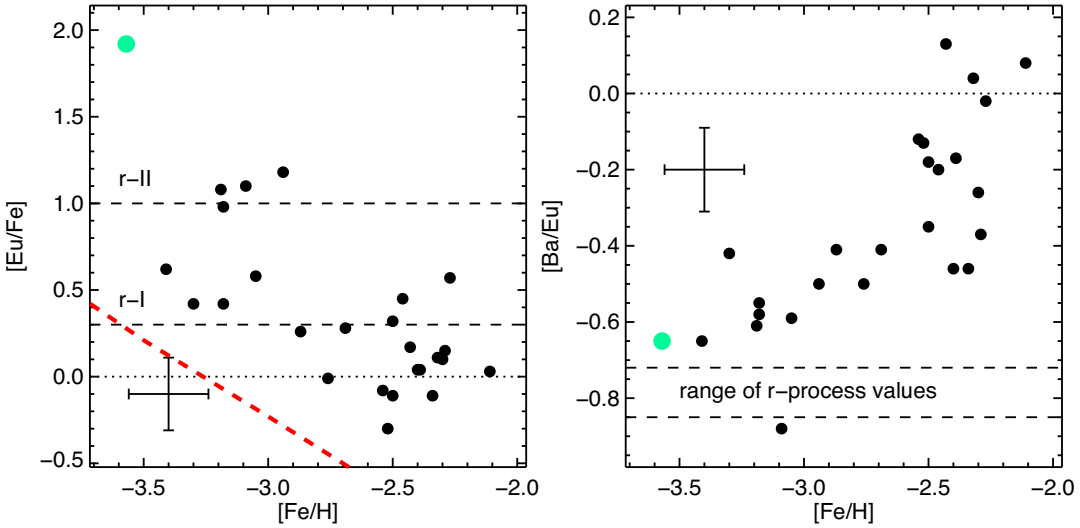

Figure 14. Left: [Eu/Fe] versus [Fe/H]. The aqua circle represents the neutron-capture rich star SMSS J200322.54−114203.3 and a representative error bar is included in the bottom left corner. The red dashed line indicates the approximate detection threshold for the 4129Å Eu II line. Right: [Ba/Eu] versus [Fe/H]. The range of scaled solar *r*-process values ([Ba/Eu] = −0.72 to −0.85) are indicated as dashed lines.

a 10 mÅ Zn I 4810.53Å line would correspond to roughly [Zn/Fe] = +0.7. Basically for a fixed $T_{\rm eff}$ and log *g*, at lower metallicities Zn measurements are only possible as the [Zn/Fe] ratio increases. The 10 mÅ value and stellar parameters were arbitrarily chosen and we regard those abundances as approximate detection thresholds. Nevertheless, the abundance dispersion appears to increase with decreasing metallicity. One object, SMSS J084327.83−141513.3, exhibits an unusually high Zn abundance with [Zn/Fe] = +1.4. We will briefly discuss this object in the following subsection.

In Fig. 14 (left-hand panel), we plot [Eu/Fe] as a function of metallicity. While the data indicate a trend of increasing [Eu/Fe] with decreasing [Fe/H], we are mindful that this is again due in part to the detection threshold for Eu. As described above for Zn, we followed the approach of Roederer (2013) and computed approximate abundance thresholds corresponding to the detection of the 4129Å Eu II line.

We identify four new r-II stars ([Eu/Fe] >+1.0 and [Ba/Eu] < 0) corresponding to 2.7 per cent of our sample that is consistent with previous studies of the frequency of such objects, ∼3 per cent (Barklem et al. 2005; Frebel 2018). We also report eight new r-I stars (0.3 ≤ [Eu/Fe] ≤ 1.0 and [Ba/Eu] < 0) that represents 5.3 per cent of our sample which is lower than the ∼15 per cent previously noted (Barklem et al. 2005; Frebel 2018). In calculating these fractions, we have assumed that the stars for which the 4129Å Eu II line is not detected are not Eu-rich. Given the estimated detection threshold for this line shown in Fig. 14, this does not seem an unreasonable assumption, particularly since the r-I and r-II fractions for only stars in which Eu is detected (8/26 r-I; 4/26 r-II) would seem unreasonably high compared to the observed fractions in other surveys (e.g. Barklem et al. 2005; Frebel 2018).

Among these Eu rich objects, we note that the r-I stars SMSS J110901.23+075441.7 and SMSS J181200.10−463148.8 are also NEMP objects. All other r-I and r-II stars are neither CEMP nor NEMP.[7]

In Fig. 14 (right-hand panel), we plot [Ba/Eu] against [Fe/H]. The data show an increase in [Ba/Eu] with increasing metallicity and this is possibly due to the contribution from the slow neutron-capture process (McWilliam 1998). The lowest values of [Ba/Eu] are consistent with the Solar system *r*-process values that range from −0.85 to −0.72 (Kappeler, Beer & Wisshak 1989). In both panels, we highlight the location of SMSS J200322.54−114203.3 that is highly enhanced in neutron-capture process elements. A comprehensive abundance analysis of this object is presented in Yong et al. (2021).

4.5 Chemically peculiar stars

4.5.1 Outliers

In Fig. 15, we plot the abundance pattern [X/Fe] for each element for 20 stars in our sample that are CEMP and/or with [Fe/H] < −3.5 as well as one 'Fe-rich' star and one low-α star. The solid line in each panel indicates the [X/Fe] ratio that a 'normal' star would have at the metallicity of each programme star. That abundance is defined using the linear fit to [X/Fe] versus [Fe/H] for which three examples are illustrated in Figs 9–11.

The red points in Fig. 15 indicate elements that depart (above or below) from the solid line by more than 0.5 dex. For C and N, the red points indicate [X/Fe] ≥ +0.7 dex (no evolutionary corrections were applied). We regard the red points as being peculiar with respect to the [X/Fe] ratio that a normal star would have at the metallicity of the programme star. This system enables us to readily identify which elements may be regarded as outliers for a given star, and therefore which stars are chemically peculiar, i.e. they exhibit multiple elements that are outliers. As noted earlier, six of the seven CEMP stars belong to the CEMP-no subclass, i.e. they have [Ba/Fe] < 0. The remaining CEMP star SMSS J030853.27−700140.1, with

[7]A more extensive chemical abundance analysis of the most iron-poor r-II star SMSS J200322.54–114203.3 using a new spectrum is presented in Yong et al. (2021). In that analysis, SMSS J200322.54–114203.3 is found to also be a NEMP object. Co-existing *r*-process and *N* enhancements might indicate an origin involving massive rotating stars and their supernovae.

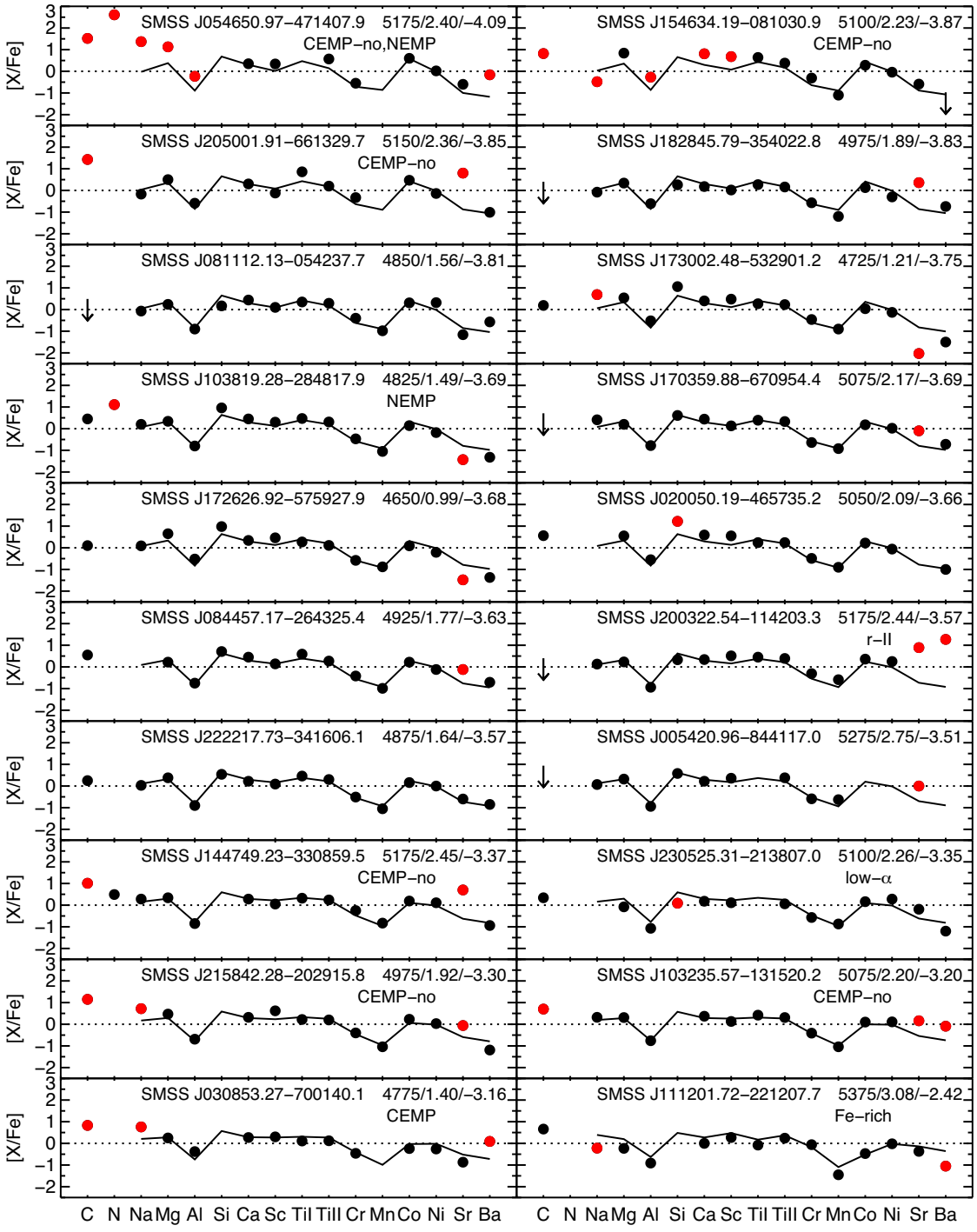

Figure 15. Abundance patterns [X/Fe] for each element for 20 programme stars that are CEMP and/or with [Fe/H] < -3.5 along with representative 'Fe-rich' and 'low-α' objects ordered by increasing metallicity. In each panel, the solid line represents the 'normal' [X/Fe] ratio at the metallicity of each programme star. The model parameters ($T_{\rm eff}$, log g, [Fe/H]) are included in each panel. Red circles indicate when [C,N/Fe] $\geq +0.7$ dex, or when [X/Fe] differs from the solid line by more than 0.5 dex.

[Ba/Fe] $= +0.09 \pm 0.17$, cannot be placed into any sub-class but when taking into account the error bars, this object could also be a CEMP-no object. As discussed in Norris et al. (2013b), CEMP objects often exhibit high abundance ratios for Na, Mg, and Al. Among the seven CEMP objects in Fig. 15, we note that four exhibit unusually high abundances for Na, Mg, and/or Al. However, for one of those objects, SMSS J154634.19−081030.9, the high Al abundances are accompanied by a low Na abundance. While the other three CEMP stars have normal Na, Mg, and Al abundances, they exhibit high Sr and/or Ba abundances when compared to the average star at the same metallicity, although they are not CEMP-*s* which have [Ba/Fe] $> +1.0$.

There are a further 13 stars that are CEMP when taking into account the evolutionary correction for carbon (Placco et al.

Table 11. Stars with [α/Fe] $\leq +0.15$ where α is the average of Mg, Si, Ca, Ti I, and Ti II and σ is the standard deviation. (As discussed in the text, the first seven stars are 'Fe-rich' while the final two are 'α-poor'.)

ID	[Fe/H] (dex)	<[α/Fe]> (dex)	σ[α/Fe] (dex)
SMSS J011126.27−495048.4	−2.94	0.06	0.07
SMSS J031703.94−374047.2	−3.27	0.13	0.15
SMSS J034749.80−751351.7	−2.50	0.04	0.32
SMSS J093524.93−715506.5	−2.48	0.13	0.16
SMSS J111201.72−221207.7	−2.42	−0.02	0.20
SMSS J170133.47−651115.6	−2.70	0.03	0.03
SMSS J190508.31−581843.9	−3.19	0.11	0.08
SMSS J230525.31−213807.0	−3.35	0.06	0.11
SMSS J232121.57−160505.4	−3.03	0.12	0.25

2014b). All belong to the CEMP-no subclass except for SMSS J054903.50−594655.4 that has [Ba/Fe] = +0.30 dex. This star does not fall into any standard CEMP subclass as the Ba abundance lies between the CEMP-no and CEMP-*s* thresholds of [Ba/Fe] < 0 and > +1, respectively. Among these objects, we note that two are also NEMP stars (SMSS J103819.28−284817.9 and SMSS J190836.24−401623.5) and one (SMSS J173002.48−532901.2) has a high Na abundance.

As noted in Yong et al. (2013b), peculiar element abundance ratios are also commonly found among the C-normal population. Among the C-normal stars (i.e. excluding CEMP with and without the evolutionary correction) at all metallicities, some 75 have at least one element from Na to Ba for which the [X/Fe] ratio differs from a normal star at the same metallicity by at least 0.5 dex (above or below). If we exclude Sr and Ba, which are known to exhibit an enormous range in [X/Fe] at low metallicity, there are some six C-normal stars that are chemically peculiar, but only SMSS J232121.57−160505.4 has more than one element that is peculiar (in this case Na and Al). Given the large sample at low metallicity, these stars that exhibit peculiar chemical abundances may represent examples of stochastic chemical enrichment.

4.5.2 *Low-α*

We identify a subset of stars which exhibit low [α/Fe] ratios, where α is the average of Mg, Si, Ca, Ti I, and Ti II. The nine objects with [α/Fe] $\leq +0.15$ are listed in Table 11, and we note that all are C-normal. For comparison, the Norris et al. (2013a) and Yong et al. (2013a) sample includes 11 giants (out of 98) with [α/Fe] $\leq +0.15$ and [Fe/H] ≤ -2.0. The frequency of low-α stars in this study, 6.0 ± 2.1 per cent, is smaller than in Yong et al. (2013a), 11.2 ± 3.6 per cent although the difference is only at the 1σ level.

Adopting the same approach as in Fig. 15, we can explore whether these nine objects appear deficient in just the α elements or whether the [X/Fe] ratios are generally low when compared to other stars at similar metallicity. In particular, we can compare the [X/Fe] ratio in each star with that of the 'typical' star at the same metallicity. For seven of these nine objects, the deficiency in α elements is essentially identical to the deficiency in all elements from Na to Ni. We therefore propose that these are 'Fe-enhanced' stars, as discussed in Cayrel et al. (2004), Venn et al. (2012), Yong et al. (2013b), and Jacobson et al. (2015). That is, the unusually low [X/Fe] ratios in these objects can most simply be explained as an excess of Fe. For these seven objects, removing ∼0.20 dex of Fe would result in [X/Fe] ratios that are typical for stars at the same metallicity.

In the study of Cordoni et al. (2021),[8] the kinematics of these seven 'Fe-enhanced' stars are quite diverse, likely indicating a variety of origins. Two stars are members of the inner Galactic halo, one is an outer-halo star, one is likely associated with the Gaia-Enceladus-Sausage accretion event (Helmi et al. 2018; Belokurov et al. 2018), two have prograde orbits in the thick-disc and one has high energy and is escaping from the Galaxy.

For the other two objects, SMSS J230525.31−213807.0 and SMSS J232121.57−160505.4, the deficiency in α elements is considerably greater than for all elements from Na to Ni. For SMSS J230525.31−213807.0, the [α/Fe] ratio differs by −0.29 dex from that for the average star at the same metallicity while for all elements from Na to Ni, the [X/Fe] differ by −0.12 dex. For SMSS J232121.57−160505.4, the same two quantities are −0.16 and +0.10 dex. We therefore propose that these two stars are α-poor and not 'Fe-enhanced'. Both of these stars have prograde orbits that are largely confined to the Galactic disc in the kinematic analysis of Cordoni et al. (2021): SMSS J230525.31−213807.0 has an orbital eccentricity of 0.58, peri- and apo-galactic distances of 2.2 and 8.4 kpc, respectively, and a maximum excursion from the Galactic plane of 2.5 kpc, while for SMSS J232121.57−160505.4, the corresponding numbers are 0.28, 5.9, and 10.4 kpc and 1.4 kpc, respectively. Given the low [Fe/H] and low [α/Fe] values for these stars (see Table 11), we speculate that they most likely originated in now disrupted low-luminosity (ultra-faint) dwarf galaxies. (See Kobayashi et al. 2014 for a more detailed discussion of the origins of low-α metal-poor stars.)

4.5.3 *SMSS J200322.54−114203.3*

As noted above SMSS J200322.54−114203.3 is the most iron-poor r-II star known: [Fe/H] = −3.57 (based on Fe I lines) and [Eu/Fe] = +1.92. A more comprehensive chemical abundance analysis of this object is presented in Yong et al. (2021) in which the *r*-process enrichment is attributed to magnetorotational hypernovae.

4.5.4 *SMSS J084327.83−141513.3*

As noted above, SMSS J084327.83−141513.3 with [Fe/H] = −3.29 is particularly enhanced in Zn with [Zn/Fe] = +1.41. For the neutron-capture elements, it has [Sr/Fe] = +1.64, [Y/Fe] = +0.69, [Zr/Fe] = +1.02, and [Ba/Fe] = −0.17. (The Eu limit is [Eu/Fe] < +0.57.) Inspection of the SAGA data base (Suda et al. 2008) indicates that among the stars with [Fe/H] < −3 it has the highest [Zn/Fe] and [Sr/Fe] ratios by about 0.20 dex, and we note that HE 1327−2326, with [Fe/H]$_{\rm NLTE}$ = −5.2, also exhibits large Zn and Sr enhancements (Ezzeddine et al. 2019). The [Sr/Ba] ratio is +1.8 which is even more extreme than the value of +1.0 reported for the ω Centauri star ROA 276 (Yong et al. 2017) in which the abundance pattern could be explained by spinstars, i.e. fast-rotating low-metallicity massive stars (Frischknecht, Hirschi & Thielemann 2012; Frischknecht et al. 2016). For SMSS J084327.83−141513.3, however, we consider the possibility that the enrichment arises from an electron-capture supernova (ECSN); a more extensive analysis of this object will be presented elsewhere (Nordlander et al. in preparation).

[8]Relative to the values presented in Cordoni et al. (2021), minor updates to the abundances have been made, but none of the conclusions of that paper are affected.

4.5.5 SMSS J165501.84−664110.7

This object is relatively metal rich with [Fe/H] = −2.52 with a very low value of [Ba/Fe] = −2.32. In Fig. 11, it notable for being about 1 dex lower in [Ba/Fe] when compared to stars at the same metallicity. However, it has only a moderately low value of [Sr/Fe] = −0.82 and appears otherwise normal in [X/Fe] ratios for all other elements except for Al where the observed and 'normal star' values are [Al/Fe] = −0.08 and −0.65, respectively.

5 CONCLUSIONS

We present chemical abundances for 21 elements from Li to Eu for a sample of 150 stars selected from the SkyMapper survey spanning −4.1 < [Fe/H] < −2.1. Our study is based on high-resolution, high-S/N spectra adopting a 1D LTE analysis. Our sample includes 90 stars with [Fe/H] ≤ −3, seven CEMP (and a further 13 when including the evolutionary correction), 11 NEMP (at least two remain NEMP if we include evolutionary mixing corrections), eight r-I and four r-II objects. Of those seven CEMP stars, six belong to the CEMP-no subclass and the other cannot be assigned to any particular subclass. One of the CEMP-no objects is also a NEMP star, and all CEMP objects lie below [Fe/H] = −3.0. Two of the NEMP stars are also r-I and one is also a CEMP-no object (SMSS J054650.97–471407.9).

We combine our sample with previous studies (Norris et al. 2013a; Yong et al. 2013a; Nordlander et al. 2019) for which there are some 177 stars with [Fe/H] ≤ −3. The metallicity distribution function has a slope of Δ(log N)/Δ[Fe/H] = 1.51 dex per dex in the range −4 ≤ [Fe/H] ≤ −3 which is comparable to the value of 1.5 ± 0.1 dex per dex in Da Costa et al. (2019) but steeper than the value of 1.0 from the Hartwick (1976) simple model. If we exclude CEMP objects, the MDF has a slope of 1.74 ± 0.02. When considering the metallicity range −3.4 < [Fe/H] < −2.7, we find the slope of the MDF is +1.07 ± 0.04 which is similar to the value of +1.0 ± 0.1 found by Youakim et al. (2020) over the range −3.4 < [Fe/H] < −2.5 in the Pristine survey. Both the present study and that of Youakim et al. (2020) find a marked turn down in the MDF at [Fe/H] ≈ –3.8; more metal-poor objects are predominantly carbon-rich.

We find that the chemical abundance ratios [X/Fe] as a function of [Fe/H] exhibit similar trends to those noted in the literature. There are two stars that are particularly unusual, and more comprehensive chemical abundance analyses are presented elsewhere: SMSS J200322.54–114203.3 is highly enhanced in the *r*-process elements and the abundance pattern could be explained by magnetorotational hypernovae (Yong et al. 2021); SMSS J084327.83–141513.3 has the highest [Zn/Fe] and [Sr/Fe] ratios among all stars with [Fe/H] < −3 in the SAGA data base and could be explained by enrichment from an electron-capture supernova (Nordlander et al. in prep).

Overall, our large and homogeneously analysed sample of metal-poor stars is a substantial contribution towards a better understanding of chemical enrichment at the earliest times. The key to constraints on the properties of the first generation of zero-metallicity stars, however, lies with the extremely rare objects for which [Fe/H] < −4; the search for such stars remains on-going.

ACKNOWLEDGEMENTS

This paper includes data gathered with the 6.5 m Magellan Telescopes located at Las Campanas Observatory, Chile. Some of the data presented herein were obtained at the W. M. Keck Observatory, which is operated as a scientific partnership among the California Institute of Technology, the University of California, and the National Aeronautics and Space Administration. The Observatory was made possible by the generous financial support of the W. M. Keck Foundation. Australian access to the Magellan Telescopes was supported through the National Collaborative Research Infrastructure Strategy of the Australian Federal Government. The authors wish to recognize and acknowledge the very significant cultural role and reverence that the summit of Maunakea has always had within the indigenous Hawaiian community. We are most fortunate to have the opportunity to conduct observations from this mountain. We thank V. Placco for providing evolutionary corrections for carbon and A. I. Karakas for helpful comments on AGB nucleosynthesis. We thank the referee for helpful comments.

Parts of this research were supported by the Australian Research Council Centre of Excellence for All Sky Astrophysics in 3 Dimensions (ASTRO 3D), through project number CE170100013. GDC acknowledges Australian Research Council grant no. DP150103294. KL acknowledges funds from the European Research Council (ERC) under the European Union's Horizon 2020 research and innovation programme (grant agreement no. 852977). ADM acknowledges Australian Research Council grant number FT160100206. AFM acknowledges support from the European Union's Horizon 2020 research and innovation programme under the Marie Sklodowska-Curie grant agreement no. 797100. ARC acknowledges Australian Research Council grant no. DE190100656. CK acknowledges funding from the UK Science and Technology Facility Council (STFC) through grant nos ST/R000905/1 and ST/V000632/1, and the Stromlo Distinguished Visitor Program at the ANU.

DATA AVAILABILITY

The data underlying this article will be shared on reasonable request to the corresponding author.

REFERENCES

Aguado D. S. et al., 2019, MNRAS, 490, 2241
Aguado D. S., Allende Prieto C., González Hernández J. I., Rebolo R., 2018, ApJ, 854, L34
Allende Prieto C., Barklem P. S., Lambert D. L., Cunha K., 2004, A&A, 420, 183
Amarsi A. M., Lind K., Asplund M., Barklem P. S., Collet R., 2016, MNRAS, 463, 1518
Aoki W. et al., 2006, ApJ, 639, 897
Aoki W., Beers T. C., Christlieb N., Norris J. E., Ryan S. G., Tsangarides S., 2007, ApJ, 655, 492
Asplund M., 2005, ARA&A, 43, 481
Asplund M., Grevesse N., Sauval A. J., Scott P., 2009, ARA&A, 47, 481
Barklem P. S. et al., 2005, A&A, 439, 129
Barklem P. S., Stempels H. C., Allende Prieto C., Kochukhov O. P., Piskunov N., O'Mara B. J., 2002, A&A, 385, 951
Baschek B., 1959, ZAp, 48, 95
Beers T. C., Christlieb N., 2005, ARA&A, 43, 531
Belokurov V., Erkal D., Evans N. W., Koposov S. E., Deason A. J., 2018, MNRAS, 478, 611
Bergemann M., Lind K., Collet R., Magic Z., Asplund M., 2012, MNRAS, 427, 27
Bernstein R., Shectman S. A., Gunnels S. M., Mochnacki S., Athey A. E., 2003, in Iye M., Moorwood A. F. M., eds, Proc. SPIE Conf. Ser. Vol. 4841, Instrument Design and Performance for Optical/Infrared Ground-based Telescopes. SPIE, Bellingham, p.1694
Bessell M. S. et al., 2015, ApJ, 806, L16
Bessell M. S., 2007, PASP, 119, 605
Bessell M. S., Norris J., 1984, ApJ, 285, 622
Bonifacio P. et al., 2009, A&A, 501, 519
Bonifacio P., Sbordone L., Caffau E., Ludwig H.-G., Spite M., González Hernández J. I., Behara N. T., 2012, A&A, 542, A87
Caffau E. et al., 2011, Nature, 477, 67

Caffau E. et al., 2020, MNRAS, 493, 4677
Casagrande L., Ramírez I., Meléndez J., Bessell M., Asplund M., 2010, A&A, 512, A54
Castelli F., Kurucz R. L., 2003, in Piskunov N., Weiss W. W., Gray D. F., eds, IAU Symp. Vol. 210, Modelling of Stellar Atmospheres. Astronomical Society of the Pacific, p. 20P
Cayrel R. et al., 2004, A&A, 416, 1117
Chamberlain J. W., Aller L. H., 1951, ApJ, 114, 52
Chiti A., Mardini M. K., Frebel A., Daniel T., 2021, ApJ, 911, L23
Christlieb N. et al., 2002, Nature, 419, 904
Clarkson O., Herwig F., 2020, MNRAS, 500, 2685
Cordoni G. et al., 2021, MNRAS, 503, 2539
Da Costa G. S. et al., 2019, MNRAS, 489, 5900
Demarque P., Woo J.-H., Kim Y.-C., Yi S. K., 2004, ApJS, 155, 667
Dopita M. et al., 2010, Ap&SS, 327, 245
Ezzeddine R. et al., 2019, ApJ, 876, 97
Frebel A. et al., 2005, Nature, 434, 871
Frebel A., 2018, Ann. Rev. Nucl. Part. Sci., 68, 237
Frebel A., Norris J. E., 2015, ARA&A, 53, 631
Frischknecht U. et al., 2016, MNRAS, 456, 1803
Frischknecht U., Hirschi R., Thielemann F.-K., 2012, A&A, 538, L2
Gaia Collaboration et al., 2021, A&A, 649, A1
Hansen T. et al., 2015, ApJ, 807, 173
Hansen C. J., Hansen T. T., Koch A., Beers T. C., Nordström B., Placco V. M., Andersen J., 2019, A&A, 623, A128
Hartwick F. D. A., 1976, ApJ, 209, 418
Helmi A., Babusiaux C., Koppelman H. H., Massari D., Veljanoski J., Brown A. G. A., 2018, Nature, 563, 85
Hollek J. K., Frebel A., Roederer I. U., Sneden C., Shetrone M., Beers T. C., Kang S.-j., Thom C., 2011, ApJ, 742, 54
Howes L. M. et al., 2015, Nature, 527, 484
Howes L. M. et al., 2016, MNRAS, 460, 884
Jacobson H. R. et al., 2015, ApJ, 807, 171
Johnson J. A., 2002, ApJS, 139, 219
Johnson J. A., Herwig F., Beers T. C., Christlieb N., 2007, ApJ, 658, 1203
Kappeler F., Beer H., Wisshak K., 1989, Rep. Prog. Phys., 52, 945
Karakas A. I., Lattanzio J. C., 2014, PASA, 31, 30
Karlsson T., 2006, ApJ, 641, L41
Kaufer A., Stahl O., Tubbesing S., Nørregaard P., Avila G., Francois P., Pasquini L., Pizzella A., 1999, Messenger, 95, 8
Keller S. C. et al., 2007, PASA, 24, 1
Keller S. C. et al., 2014, Nature, 506, 463
Kelson D. D., 2003, PASP, 115, 688
Kobayashi C., Nakasato N., 2011, ApJ, 729, 16
Kobayashi C., Karakas A. I., Umeda H., 2011, MNRAS, 414, 3231
Kobayashi C., Ishigaki M. N., Tominaga N., Nomoto K., 2014, ApJ, 785, L5
Kobayashi C., Karakas A. I., Lugaro M., 2020, ApJ, 900, 179
Kurucz R. L., Bell B., 1995, Atomic Line List. Smithsonian Astrophysical Observatory, Cambridge, MA
Lawler J. E., Wickliffe M. E., den Hartog E. A., Sneden C., 2001, ApJ, 563, 1075
Li H. N. et al., 2010, A&A, 521, A10
Lind K., Bergemann M., Asplund M., 2012, MNRAS, 427, 50
Marino A. F. et al., 2019, MNRAS, 485, 5153
Mashonkina L., Gehren T., Shi J. R., Korn A. J., Grupp F., 2011, A&A, 528, A87
McWilliam A., 1998, AJ, 115, 1640
McWilliam A., Preston G. W., Sneden C., Searle L., 1995, AJ, 109, 2757
Nomoto K., Kobayashi C., Tominaga N., 2013, ARA&A, 51, 457
Nordlander T. et al., 2019, MNRAS, 488, L109
Nordlander T., Amarsi A. M., Lind K., Asplund M., Barklem P. S., Casey A. R., Collet R., Leenaarts J., 2017, A&A, 597, A6
Norris J. E. et al., 2013a, ApJ, 762, 25
Norris J. E. et al., 2013b, ApJ, 762, 28
Norris J. E., Christlieb N., Korn A. J., Eriksson K., Bessell M. S., Beers T. C., Wisotzki L., Reimers D., 2007, ApJ, 670, 774
Norris J. E., Gilmore G., Wyse R. F. G., Yong D., Frebel A., 2010, ApJ, 722, L104
Onken C. A. et al., 2019, PASA, 36, e033
Placco V. M., Frebel A., Beers T. C., Christlieb N., Lee Y. S., Kennedy C. R., Rossi S., Santucci R. M., 2014a, ApJ, 781, 40
Placco V. M., Frebel A., Beers T. C., Stancliffe R. J., 2014b, ApJ, 797, 21
Placco V. M., Frebel A., Lee Y. S., Jacobson H. R., Beers T. C., Pena J. M., Chan C., Heger A., 2015, ApJ, 809, 136
Prantzos N., 2008, A&A, 489, 525
Ramírez I., Allende Prieto C., Lambert D. L., 2008, A&A, 492, 841
Reggiani H., Meléndez J., Kobayashi C., Karakas A., Placco V., 2017, A&A, 608, A46
Roederer I. U., 2013, AJ, 145, 26
Roederer I. U., Preston G. W., Thompson I. B., Shectman S. A., Sneden C., Burley G. S., Kelson D. D., 2014, AJ, 147, 136
Ryan S. G., Norris J. E., Beers T. C., 1996, ApJ, 471, 254
Salvadori S., Schneider R., Ferrara A., 2007, MNRAS, 381, 647
Schneider R., Ferrara A., Salvaterra R., Omukai K., Bromm V., 2003, Nature, 422, 869
Schörck T. et al., 2009, A&A, 507, 817
Simpson J. D., Martell S. L., 2019, MNRAS, 490, 741
Sneden C., 1973, ApJ, 184, 839
Sobeck J. S. et al., 2011, AJ, 141, 175
Spite M. et al., 2005, A&A, 430, 655
Starkenburg E. et al., 2017, MNRAS, 471, 2587
Starkenburg E. et al., 2018, MNRAS, 481, 3838
Suda T. et al., 2008, PASJ, 60, 1159
Thévenin F., Idiart T. P., 1999, ApJ, 521, 753
Tominaga N., Iwamoto N., Nomoto K., 2014, ApJ, 785, 98
Venn K. A. et al., 2012, ApJ, 751, 102
Venn K. A. et al., 2020, MNRAS, 492, 3241
Venn K. A., Irwin M., Shetrone M. D., Tout C. A., Hill V., Tolstoy E., 2004, AJ, 128, 1177
Vogt S. S. et al., 1994, in Crawford D. L., Craine E. R., eds, SPIE Conf. Ser. Vol. 2198, Instrumentation in Astronomy VIII. SPIE, Bellingham, p. 362
Wallerstein G., Greenstein J. L., Parker R., Helfer H. L., Aller L. H., 1963, ApJ, 137, 280
Wang E. X., Nordlander T., Asplund M., Amarsi A. M., Lind K., Zhou Y., 2021, MNRAS, 500, 2159
Yong D. et al., 2013a, ApJ, 762, 26
Yong D. et al., 2013b, ApJ, 762, 27
Yong D. et al., 2021, Nature, 595, 223
Yong D., Norris J. E., Da Costa G. S., Stanford L. M., Karakas A. I., Shingles L. J., Hirschi R., Pignatari M., 2017, ApJ, 837, 176
Yoon J. et al., 2016, ApJ, 833, 20
Youakim K. et al., 2020, MNRAS, 492, 4986

SUPPORTING INFORMATION

Supplementary data are available at *MNRAS* online.

supplementary_table.txt

Table S1. Programme stars and observing details.
Table S2. Line list and equivalent width measurements.
Table S3. Model atmosphere parameters.
Table S5. Carbon abundances and the corrections for evolutionary status from Placco et al. (2014b).
Table S7. Chemical abundances (Na-Ba) for the programme stars.
Table S8. Chemical abundances for Zn, Y, Zr and Eu.
Table S9. Abundance errors from uncertainties in atmospheric parameters.
Table S10. Abundances and stellar parameters for all stars.

Please note: Oxford University Press is not responsible for the content or functionality of any supporting materials supplied by the authors. Any queries (other than missing material) should be directed to the corresponding author for the article.

This paper has been typeset from a TEX/LATEX file prepared by the author.